Theoretical Structural Design of Uneven Coating Thickness of Catalyst Layer in Polymer Electrolyte Fuel Cell

盧, 太炯

Theoretical Structural Design of Uneven Coating Thickness of Catalyst Layer in Polymer Electrolyte Fuel Cell

令和六年度　博士論文

九州大学大学院工学府　化学システム工学専攻

第 7 講座　TAE HYOUNG NOH

2024 年 6 月

Theoretical Structural Design of Uneven Coating Thickness of Catalyst Layer in Polymer Electrolyte Fuel Cell

令和六年度　博士論文

九州大学大学院工学府　化学システム工学専攻

第 7 講座　TAE HYOUNG NOH

2024 年 6 月

Contents

1. Introduction

1.1 Research Background

With the continuous development of economy in the 21st century, the demand for automobiles and other traffic tools has been rapidly increasing. Fossil fuels such as coal and oil are extensively exploited by people, leading to the currently observed depletion of fossil energy [1]. Moreover, the excessive use of fossil energy by human beings has emerged as the primary source of greenhouse gas emissions, such as carbon dioxide and nitrogen dioxide emissions, which are gradually the increasing greenhouse effect on Earth [2-3]. Therefore, owing to the soaring demand for autonomous vehicles, researchers have shifted their focus from traditional fossil fuels and are now investigating new types of energies, such as solar energy and nuclear energy, to reduce the use of fossil energy and greenhouse gas emissions [4].

Fuel cells are eco-friendly systems that generate water as a by-product while producing electricity, and the ideal reaction product is solely water [5] . The working principle of fuel cell represents in **Fig 1.1**. Usually, the fuel energy generation process includes the following four steps:

1) Burning of fuel to convert chemical energy into heat.
2) Using this heat to increase the water temperature and generate steam.
3) Using this steam to drive a turbine, and during this process, heat is converted into mechanical energy.
4) Finally, this generated mechanical energy can be used to drive a generator that can generate electricity.

Fuel cells can avoid all the aforementioned process steps and generate electricity without requiring mechanical moving parts in the fuel cell body [6]. This simplified functioning of fuel cells has garnered considerable attention from researchers. As shown in **Fig. 1.2,** the fuel cell market size is anticipated to continuously grow from 2021 to 2032 [7]. Fuel cells can be classified into several types according to the reactants, electrolytes, and operating temperatures. **Table 1.1** lists six types of fuel cells [8-10]. Fuel cells can directly transform chemical energy into electrical energy, and a continuous

fuel and oxidant supply, which is critical to sustain the power generation capability of fuel cells, enables the formation of a clean product, facilitates cogeneration because of on-site power generation, and allows low noise generation [11]. Therefore, a fuel cell is a highly promising energy generation technology. Among the fuel cells reported to date, a solid polymer electrolyte fuel cell (PEFC) utilizes a fluorine-based cation exchange membrane in the electrolyte. A thin-film-based strongly acidic gel electrolyte exhibits a high ionic conductivity even at temperatures close to the room temperature, can operate at low temperatures, and can start at room temperature owing to its ability to withstand differential pressure. Furthermore, because the reaction sites of hydrogen and oxygen can be well designed, PEFCs can be miniaturized and exhibit a high output power density, as shown in **Fig. 1.3.** However, owing to the strongly acidic nature of the membrane, a highly corrosion resistant electrode catalyst material is required, which is the disadvantage of PEFCs. Furthermore, a thin membrane exhibits insufficient heat resistance and mechanical strength, and consequently, the requirements for processing accuracy are stringent. As mentioned before, triggered by the necessity of developing an alternative fuel utilization technology, experts are gradually shifting their focus from gasoline to PEFCs to power automobiles. However, the absence of suitable methods for constructing low-cost and highly durable PEFCs, characterized by low activation energies, is the primary issue impeding the large-scale application of PEFCs.

1.2 The Structure and Principle of PEFCs

As shown in **Fig. 1.1**, a single PEFC is composed of a gas diffusion layer (GDL), a separator with gas supplied to the groove, and a membrane electrode assembly (MEA) with a current collector sandwiching a PEM, which is in turn sandwiched by two catalyst layers. Each electrode exhibits a two-layer structure composed of a catalytic layer and a GDL. In actual reaction conditions, a hydrophobic layer is often provided on the GDL to control the moisture level in the electrode. In the PEFC reaction, hydrogen and oxygen serve as the fuel and oxidant, respectively, and the cell typically operates at a low-temperature range of 60–100 ℃. The following main reactions occur on the surface of catalyst that connects the electrolyte and membrane:

Anode: $2H_2 \rightarrow 4H^+ + 4e^-$ (1.1)

Cathode: $4H^+ + O_2 + 4e^- \rightarrow 2H_2O$ (1.2)

Total: $2H_2 + O_2 \rightarrow 2H_2O$ (1.3)

At the anode, the hydrogen gas fuel undergoes (**Eq. 1.1**) in the catalyst layer, decomposing into protons and electrons. The protons traverse the PEM, while the electrons propagate to the cathode through an external current loop. At the cathode, electrons and protons supplied by the anode side and the oxygen supplied from air trigger the oxygen reduction reaction (ORR; **Eq. 1.2**). Ideally, as shown in **Eq. 1.3**, the total reaction product of the fuel cell is only water. These reactions result in the flow of a direct current through an external current loop. Although some side reactions also occur, the operational process of a PEFC can be accurately described by the aforementioned equations. The smallest unit of a fuel cell is called a single cell, and because the voltage of a single fuel cell is ~0.7 V, multiple single batteries in series are often used.

1.3 Component of PEFCs

This section introduces the materials of PEFC components, which include an electrode catalyst layer, an electrolyte polymer (an ionomer), a PEM, a gas diffusion substrate, and a separator. Among these, the PEM, sandwiched between two porous electrodes, is the main component of a PEFC. Porous electrodes are required to ensure that the reactant gas, which is supplied from the back side, reaches the electrolyte–membrane interface and reacts on the catalyst's surface. An MEA, sandwiched the collector and separator, is configured between the two electrodes. The collector mainly collects and conducts current, whereas the separator separates the gases into two adjacent cells. The materials used in our experiment and those assumed for the calculations are summarized in **Table 1.2**.

1.3.1 Polymer Electrolyte Membrane

The polymer electrolyte membrane (PEM) utilized in PEFCs should:

1) allow free movement of protons,

2) prevent direct reaction between oxygen and hydrogen,

3) do not conduct electrons between the cathode and anode, and

4) exhibit high stability, water mobility, and temperature resistance.

Currently, perfluorosulfonic acid (PSA) ionic polymers, which are essentially copolymers of tetrafluoroethylene and different perfluorosulfonic monomers as well as exhibit these properties, are considered the most suitable membranes. Among the several known perfluorosulfonated membranes, Nafion™ films developed by DuPont, a USA-based chemical company, in the 1960s, are the most utilized membranes in fuel cells. This membrane is composed of perfluorosulfurethyl–propyl–vinyl ether, and the chemical structure of PSA ionic polymer is depicted in **Fig. 1.4**, Nafion consists of a perfluorosulfonate polymer (PSAP) with a continuous hydrophilic basis containing sulfonate (SO_3H) and to some extent a $–(CF_2)_n–$ skeleton; PSAP is called an ionic polymer owing to the electrovalent bonding of the SO_3H radical [12-14]. The side-chain end tends to congregate in the overall structure of the membrane owing to the ionic property. Although the Teflon main chain is hydrophilic, the sulfonic acid in the side-chain end is hydrophobic, and thus, this material can adsorb relatively large amounts of water. With the flow of H^+ ion through this membrane, which adsorbs a large amount of water, leading to proton conduction in the material. When the PEM is in a water-containing state, sulfonic acid dissociates and shows a relatively high proton conductivity at 80 °C. Consequently, the proton conductive of a PEM is 3–4 times higher than that of other ion-exchange membranes.

Because the ohmic loss of a PEM affects the performance of fuel cells, thinner membranes have been developed for realizing high current densities. A PEM acts as an electrolyte as well as a bulkhead, dividing the inside of the cell into anode and cathode sides. An extremely thin PEM cannot function as an efficient bulkhead; in this case, crossover of the supply gas occurs, and hydrogen and oxygen react directly, leading to a decrease in the cell's efficiency. Therefore, PEMs need to have some thickness [15-17].

1.3.2 Gas Diffusion Layer

The catalyst layer and current path of the PEFC are connected by a gas diffusion layer (GDL), which

determines the utilization rate and overall performance of the catalyst. Although the GDL does directly participate in the chemical reactions, it has several critical functions in PEFCs:

1) It acts as a supply pathway for the reactive gas from the stream field channel to the catalyst layer, facilitating the incorporation of the gas into the whole active area.
2) It provides a supply pathway for the generated water from the catalyst layer to the stream filed channel.
3) It combines the catalyst layer and bipolar plane to form a complete circuit for electrons.
4) It conducts the heat generated from the electrochemical reactions in the catalyst layer to the bipolar plane, thereby providing a cooling route.
5) It provides mechanical support to the MEA, thus preventing it from drooping to the stream field channel.

Thus, according to these functions, the GDL should possess the following characteristics:

1) It must be porous to allow the passage of reactive gases and the generated water.
2) It must be conductive and can transfer heat within the plane. Interface resistance or contact resistance is usually more important than volume conductivity.
3) The size of the holes in the catalyst-layer side should not exceed those of the particles dispersed to form the catalyst layer.
4) It should exhibit good stiffness to support the MEA as well as ensure good electrical contacts.

To fulfil these aforementioned requirements, the gas diffusion substrate uses a 0.2 mm thick porous carbon material, such as non-woven carbon fiber fabric; specifically, carbon materials heat-treated at a temperature above ~2000 °C, with high air permeability and a high electronic conductivity, is used [18-21]. In PEFCs, when humidified hydrogen and oxygen are supplied to the anode and cathode, respectively, to generate electricity, the GDL should act as a conductive pathway for electrons from the separator to the catalyst layer; hydrogen, oxygen, and water vapor should also be conducted by the GDL from the gas flow path of the separator to the catalyst layer; in addition, the reactant water should be transported from the cathode catalyst layer (CCL) to the separator by the GDL.

1.3.3 Bipolar Plate

To connect a fuel cell in series, each single cell is separated from the next cell by an electron conductive bipolar plate (separator) that plays an interconnecting role. This bipolar plate is usually required as a gas flow path or current collection plate in a single cell. The separator has flow channels on both sides, and one of its roles is to transport the raw material gas, water vapor, and liquid water to the electrodes. In addition, this flow path removes water vapor and the generated heat. Therefore, the design of bipolar plates and configuration of the flow channels have been extensively studied in various fields as shown in **Fig. 1.5.** Plate topologies and materials may include straight, winding, or mutually digitized flow fields, along with internal manifolds, internal humidification, and integrated cooling. Bipolar plates should ensure uniform distribution of the reaction gases on the active electrode surface to minimize concentration overpotential as well as exhibit a high electronic conductivity for current collection, a high mechanical strength for stack integrity, impermeability to reactant gases for safe operation, and resistance to corrosion in extreme cell environments during long-term fuel cell operation [22–23]. Carving or milling is the most common method of manufacturing fluid flow channels on bipolar plate surfaces.

1.3.4 Electrode

The electrode of a PEFC is virtually a catalyst layer that connects the PEM with a conductive porous board. In the electrochemical reactions occurring on the catalyst's surface, three components are involved, and all three components must access to the reaction site. In particular, electrons pass through the conductive particles, including the catalyst itself, whereas the protons travel through the ionomer; thus, the catalyst must be correlated with the ionomer. Lastly, the reactant gas can simply flow through the void space, and thus, the electrode must be porous to ensure flow of gas toward the reaction site.

Pt is the best catalyst for oxygen reduction reaction (ORR) and hydrogen oxidation reaction (HOR). Normally, a higher Pt loading is generally used in the cathodes because the ORR in the cathodes is much slower than the HOR in the anode. In the early days of the development of fuel cells, large

amounts of Pt catalysts were used to reduce the activation energy of the fuel cells. However, recently, an electrode manufacturing method that induces a sufficient electrochemical reaction with only 0.1 mg/cm^2 catalyst has been developed to improve the performance [24-26].

Figure 1.6 shows the cross-sectional view of the catalyst layer at the cathode. Evidently, the catalyst layer has a porous structure and consists of a Pt/C support and an ionomer. The catalyst layer normally ranges from 10–50 nm in thick, and the Pt particles with sizes of 1–5 nm are highly dispersed on the carbon support. Both carbon and Pt are covered with an ionomer, which is responsible for conducting protons.

To minimize the cell potential loss due to proton migration and reactive gases that filter into the CCL, a thin catalyst layer is required. Further, the Pt active surface area should be maximized at smallest possible Pt loading is utilized. Normally, a large Pt to carbon ratio (Pt/C) should be used (40 %); however, as the smaller Pt particles are used, the lower Pt/C can be used due to the Pt active area is higher. Therefore, the key to increase cell properties is to increase the Pt utilization in catalyst layer.

1.3.5 Membrane Electrode Assembly

The membrane-electrode assembly (MEA), the most important component that determines the performance of a fuel cell, is constructed by bonding porous electrodes on both sides of a polymer electrolyte membrane (PEM). A substantial electrochemical reaction occurs in this structure, which determines the performance of the fuel cell. At the anode, hydrogen comes in contact with the Pt catalysts, decomposing into hydrogen ions and electrons, and the generated hydrogen ions travel to the cathode through the electrolyte membrane. The generated electrons move to the cathode through an external circuit, and the hydrogen ions react with oxygen, generating water.

1.4 The Relationship between Current Density Characteristics and Energy

The output density is the energy extracted per unit volume of the fuel cell and is numerically expressed as the product of the current density (current value per unit area) and cell voltage. The higher

the output density, the smoother the operation of the fuel cell, which requires a high output, such as initial acceleration.

Figure 1.7 shows the relationship between fuel cell performance and overvoltage. If an actual fuel cell is used to extract electricity, then as the current density increases, the cell voltage drops below the standard electromotive force; this voltage loss is called overvoltage, which is generally perceived to be caused by the following factors:

1) Activation overvoltage: Activation overvoltage occurs when the reaction on the surface of the electrode is delayed. This voltage is used to overcome an activation barrier to facilitate an electrochemical reaction, in which electrons are either moved to the electrode or moved from the electrode.
2) Ohmic overvoltage: Ohmic overvoltage refers to the voltage loss caused by the electrical resistance of the electrode and the resistance of the electrolyte to ion flow. This resistance includes the contact resistance generated by the fuel cell and bipolar plates, but most of the ohmic overvoltage is caused by electrolyte resistance.
3) Mass transport overvoltage: If oxygen, which is the fuel, is supplied to the fuel cell cathode in the form of air, oxygen is used in electrochemical reactions inside the fuel cell, and the concentration of oxygen is slightly reduced near the electrode. This change in concentration causes the partial pressure of oxygen to decrease. Additionally, when hydrogen is supplied to the fuel cell anode, it is divided into hydrogen ions and electrons, and a current flows into the cell, resulting in a slight reduction in hydrogen concentration. In such cases, a decrease in the partial pressure of the fuel causes a decrease in the voltage. The pressure of the reactant changes due to the voltage reduction, and as a result, the cell voltage is changed.

Figure 1.7 confirms that the voltage efficiency (ratio of fuel cell voltage to standard electromotive force) is high when the fuel cell is operated at a low current density. Due to these characteristics, the power generation efficiency is high even with partial loading.

This study was also focused on the current–voltage (I–V) performance of the PEFC in the practical voltage region during its operation; in addition, the transport of reactants was analyzed. A large

electrode area is required to obtain a predetermined current value during low current density operation, which increases the fuel cell cost. Therefore, a reasonable fuel cell utilization rate and high fuel cell voltage at a high current density are the conditions for realizing highly efficient power generation. This study also focused on I-V performance in the practical voltage region during operation and analyzed the transport of reactants.

1.5 Previous Approach for Improving Cell Performance

Two major issues, high costs and poor performance/durability of PEFCs, hinder the popularization and expansion of fuel cell vehicles. High cost is the most important issue because the ORR that occurs at the cathode is a rate-determining reaction [27-29], the reaction rate is lower than that of the reaction that occurs at the anode; therefore, the cathode needs to consume a large amount of Pt, which is expensive. **Figure. 1.8** shows the fuel cell cost breakdown, indicating that owing to the high cost of the Pt catalyst, reducing the overall cost of the system is challenging. To expand the spread of PEFC, further cost reduction of the entire system is required. Therefore, it is necessary to consider the development of low Pt catalyst and non-Pt catalyst, and the catalyst layer structure that allows Pt to be used with high efficiency.

To increase the utilization rate of Pt, it is necessary to supply the various reaction species smoothly, quickly and uniformly; that is, developing methods to optimize the structure of cathode catalyst layer is crucial. Improving oxygen diffusion and proton conductivity are promising approach to enhance the ORR.

1.5.1 Previous Studies in the Enhancement of Oxygen Diffusion

Oxygen diffusion is a dominant factor affecting current limiting density because resistance occurs when oxygen transport in void space and in ionomer. Ott et al. [30] reported that a uniformly controlled ionomer film with consistent thickness enhances oxygen diffusion performance through void spaces. Novitski et al. experimentally assessed oxygen transport properties in ionomer under various humid conditions. The improvement of PEFC performance when considering O_2-He can be attributed to a higher oxygen diffusion when oxygen in helium is used as gas reactant. Notably, the oxygen diffusion

in this type of catalyst is inhibited. Increased back pressure significantly boosts the performance of the cell, which indicates a mass transport issue. This range successfully captures all frequencies at which fast processes such as the hydrogen oxidation reaction and proton transport, and slow processes such as oxygen diffusion and the oxygen reduction reaction occur [31-33]

The presence of liquid water is also important factor that contribute to the oxygen diffusion resistance because the water liquid occupied the void space. Thus, controlling water removal will help to lower the oxygen diffusion. Uchida et al. reduced the amount of remaining liquid water in the catalyst layer using hydrophobic polytetrafluoroethylene (PTFE) particles [34]. Increase oxygen diffusion through water management can be not only in catalyst layers itself, but in the GDL. [35] used hydrophobic and hydrophilic GDL, and the results showed that pores formed in the hydrophobic region, and oxygen diffusion was enhanced.

Other ways to improve the oxygen diffusion is to increase the surface area for oxygen accessibly. Accordingly, several 3D patterns of catalyst layers have been made [36-37], in these, study the cell performance significantly improve compared to conventional flat catalyst layers.

1.5.2 Previous Studies in the Enhancement of Proton Conduction

A cell with good electrochemical properties enables proton conductivity from the PEM to the GDL. Therefore, the conductivity of protons can be increased under a high humidity condition, which allows the behavior of water in the liquid state to be identified within the catalyst layer. Consequently, studies on improving proton conductivity have been widely conducted. In one of the reported conductivity improvement methods, the side chain length is shortened to increase in the ion exchange capacity, which is one of the essential factors determining proton conductivity. A comparison of the conductivities and gas permeabilities of several membranes with short and long side chains as well as with ion-exchange capacities of 0.66–1.35 mmol/g was performed in a previous study [38]. In addition to optimizing existing materials, the development of new membrane materials has been a significant area of research. Composite membranes combining organic and inorganic components have been investigated for their potential to offer better proton conduction and durability [39-40].

1.6 Purpose of Study

The aforementioned studies have primarily concentrated on either enhancing oxygen diffusion or improving proton conduction in PEFCs. However, methods to improve oxygen diffusion and proton conductivity simultaneously have not yet been explored. Therefore, in this study, we attempted to improve both oxygen diffusion and proton conductivity in PEFCs. Inspired by 3D structure of lithium-ion battery as seen in **Fig. 1.9**, 3D structures can increase the effective reaction interface and reduce the ion transport distance with lithium-ion batteries, but 3D structures can increase charging and discharging performance under higher conditions than without 3D structures. However, improve oxygen diffusion and proton conductivity simultaneously have not yet been explored. Therefore, in this study, the structure of the cathode catalyst layer was modified to optimize proton, electron and oxygen transport paths to improve cell performance.

In experiment, we designed CCL structures with short proton conduction paths and supplemented them with sufficient ionomers by adding the ionomer layer (IL). First, using theoretical equations, we confirmed that the shortened path of proton conduction in the IL with a 3D-patterned structure compared to that in the IL with a flat-patterned structure can improve the cell performance. We experimentally investigated the effect of 3D-patterned ILs included in CCLs on the cell performance. To fabricate this structure, we coated the single side or double side 3D patterns using the inkjet printing method as shown in **Fig. 1.10**. Various CCL structures obtained by combining the IL and catalyst layer (CL) were analyzed and electrochemically evaluated at 80 °C and 100 % and 40 % RHs. Because it is difficult to measure the distribution of spices transport within CCL in experiments, we performed the numerical simulation of 3D double side structure. In particular, the flat, 3D and 3D double side structures are simulated that similar in experiment. In addition, the optimized design of 3D-pattern structure with additional ILs is investigated by changing the configuration of ionomer layer.

Reference:

[1] I. Capellán-Pérez, M. Mediavilla, C. de Castro, Ó. Carpintero, L.J. Miguel, Fossil fuel depletion and socio-economic scenarios: An integrated approach, Energy. 77 (2014) 641–666. https://doi.org/10.1016/j.energy.2014.09.063.

[2] T. A. Gottschalk *et al*., Mobility 2030: Meeting the Challenges to Sustainability, Chapter 2, World Business Council for Sustainable Development (WBCSD), pp. 25-64.

[3] C. Garrett, Progress in Energy and Combustion ence, 369, 18 (1992).

[4] S.A. Miller, Sustainable polymers: Replacing polymers derived from fossil fuels, Polym. Chem. 5 (2014) 3117–3118. https://doi.org/10.1039/c4py90017k.

[5] D. Bevers, N. Wagner, M. Von Bradke, Innovative production procedure for low cost PEFC electrodes and electrode/membrane structures, Int. J. Hydrogen Energy. 23 (1998) 57–63. https://doi.org/10.1016/s0360-3199(97)00028-1.

[6] J. Larminie, A. Dicks, Fuel Cell Systems Explained, second ed., 2013, https:// doi.org/10.1002/9781118878330.

[7] https://www.gminsights.com/

[8] Lex, P.; Jonshagen, B.: 'The zinc/bromine battery system for utility and remote area applications', Power Engineering Journal, 1999, 13, (3), p. 142-148, https://doi.org/10.1049/19990307

[9] S.D. Knights, K.M. Colbow, J. St-Pierre, D.P. Wilkinson, Aging mechanisms and lifetime of PEFC and DMFC, J. Power Sources. 127 (2004) 127–134. https://doi.org/10.1016/j.jpowsour.2003.09.033.

[10] Rajendran, Raj G. "Polymer electrolyte membrane technology for fuel cells." MRS bulletin 30.8 (2005): 587-590.

[11] J. Peron, A. Mani, X. Zhao, D. Edwards, M. Adachi, T. Soboleva, Z. Shi, Z. Xie, T. Navessin, S. Holdcroft, Properties of Nafion® NR-211 membranes for PEMFCs, J. Memb. Sci. 356 (2010) 44–51. https://doi.org/10.1016/j.memsci.2010.03.025.

[12] Dupont, Nafion®; PFSA Membranes N115, N117, N110 Datasheet. www2.dupont.com/FuelCells/en_US/assets/downloads/dfc101.pdf.

[13] Dupont, Nafion®; PFSA Membranes NR211 and NR212 Datasheet. www2.dupont.com/FuelCells/en_US/assets/downloads/dfc201.pdf

[14] S. Hamrock, Membranes and MEAs for Dry, Hot Operating Conditions, *DOE Hydrogen and Fuel Cells Program.*, 662 (2011).

[15] T.A. Zawodzinski, C. Derouin, S. Radzinski, R.J. Sherman, V.T. Smith, T.E. Springer, S. Gottesfeld, Water Uptake by and Transport Through Nafion® 117 Membranes, J. Electrochem. Soc. 140 (1993) 1041–1047. https://doi.org/10.1149/1.2056194.

[16] OS. Burheim, Thermal Signature and Thermal Conductivities of PEM Fuel Cells, Ph.D.

Thesis (2009).

[17] Sinha, P. K., Mukherjee, P. P., & Wang, C. Y. "Impact of GDL structure and wettability on water management in polymer electrolyte fuel cells." Journal of Materials Chemistry 17.30 (2007): 3089-3103. https://doi.org/10.1039/B703485G.

[18] P. Chippar, O. Kyeongmin, K. Kang, H. Ju, A numerical investigation of the effects of GDL compression and intrusion in polymer electrolyte fuel cells (PEFCs), Int. J. Hydrogen Energy. 37 (2012) 6326–6338. https://doi.org/10.1016/j.ijhydene.2011.04.154.

[19] K.S.S. Naing, Y. Tabe, T. Chikahisa, Performance and liquid water distribution in PEFCs with different anisotropic fiber directions of the GDL, J. Power Sources. 196 (2011) 2584–2594. https://doi.org/10.1016/j.jpowsour.2010.10.080.

[20] X. Li, I. Sabir, Review of bipolar plates in PEM fuel cells: Flow-field designs, Int. J. Hydrogen Energy. 30 (2005) 359–371. https://doi.org/10.1016/j.ijhydene.2004.09.019.

[21] A. Hermann, T. Chaudhuri, P. Spagnol, Bipolar plates for PEM fuel cells: A review, Int. J. Hydrogen Energy. 30 (2005) 1297–1302. https://doi.org/10.1016/j.ijhydene.2005.04.016.

[22] K. Petrovl, B. Miadenova, S. Gamburzev, A. John Appleb, P. Napolitano, P. Atanassova, M. Hampden-Smith, Evaluation of polymer electrolyte fuel cell catalysts using gas diffusion electrodes in aqueous electrolytes, Bulg. Chem. Commun. 40 (2008) 333–339..

[23] S.C. Ball, S.L. Burton, E. Christian, A. Davies, J. Fisher, R. O'Malley, S. Passot, B.C. Tessier, B. Theobald, D. Thompsett, Activity and Stability of Pt Monolayer Core Shell Catalysts, ECS Meet. Abstr. MA2009-02 (2009) 982–982. https://doi.org/10.1149/ma2009-02/10/982.

[24] Y.T. Pan, D. Li, S. Sharma, C. Wang, M.J. Zachman, E.C. Wegener, A.J. Kropf, Y.S. Kim, D.J. Myers, A.A. Peterson, D.A. Cullen, J.S. Spendelow, Ordered CoPt oxygen reduction catalyst with high performance and durability, Chem Catal. 2 (2022) 3559–3572. https://doi.org/10.1016/j.checat.2022.10.030.

[25] W. Yoon, A.Z. Weber, Modeling Low-Platinum-Loading Effects in Fuel-Cell Catalyst Layers, J. Electrochem. Soc. 158 (2011) B1007. https://doi.org/10.1149/1.3597644.

[26] T. Suzuki, K. Kudo, Y. Morimoto, Model for investigation of oxygen transport limitation in a polymer electrolyte fuel cell, J. Power Sources. 222 (2013) 379–389. https://doi.org/10.1016/j.jpowsour.2012.08.068.

[27] J. Marcinkoski, J. Spendelow, A. Wilson, D. Papageorgopoulos, P. Reviewed, R. Ahluwalia, B. James, C. Houchins, J. Moton, DOE Hydrogen and Fuel Cells Program Record, DOE Hydrog. Fuel Cells Progr. Rec. Rec. (2015) 15015. https://www.hydrogen.energy.gov/pdfs/15015_fuel_cell_system_cost_2015.pdf.

[28] W. Yoshimune, M. Harada, Effect of Pt loading on the adsorption of perfluoro-sulfonic acid ionomer in catalyst ink for polymer electrolyte fuel cells, Chem. Lett. 48 (2019) 487–490. https://doi.org/10.1246/cl.190017.

[29] R. Balu, N.R. Choudhury, J.P. Mata, L. De Campo, C. Rehm, A.J. Hill, N.K. Dutta, Evolution of the Interfacial Structure of a Catalyst Ink with the Quality of the Dispersing Solvent: A Contrast Variation Small-Angle and Ultrasmall-Angle Neutron Scattering Investigation, ACS Appl. Mater. Interfaces. 11 (2019) 9934–9946. https://doi.org/10.1021/acsami.8b20645.

[30] S. Ott, A. Orfanidi, H. Schmies, B. Anke, H.N. Nong, J. Hübner, U. Gernert, M. Gliech, M. Lerch, P. Strasser, Ionomer distribution control in porous carbon-supported catalyst layers for high-power and low Pt-loaded proton exchange membrane fuel cells, Nat. Mater. 19 (2020) 77–85. https://doi.org/10.1038/s41563-019-0487-0.

[31] M.B. Karimi, K. Hooshyari, P. Salarizadeh, H. Beydaghi, V.M. Ortiz- Martínez, A. Ortiz, I. Ortiz Uribe, F. Mohammadi, A comprehensive review on the proton conductivity of proton exchange membranes (PEMs) under anhydrous conditions: Proton conductivity upper bound, Int. J. Hydrogen Energy. 46 (2021) 34413–34437. https://doi.org/10.1016/j.ijhydene.2021.08.015.

[32] Y. Tabe, M. Nishino, H. Takamatsu, T. Chikahisa, Effects of Cathode Catalyst Layer Structure and Properties Dominating Polymer Electrolyte Fuel Cell Performance, J. Electrochem. Soc. 158 (2011) B1246. https://doi.org/10.1149/1.3624606.

[33] S.G. Compton, S.G. Beesley, D.A. Jones, Variation in the colour of the keel petals in lotus corniculatus L. 5. successional differences in the distribution of dark-keeled plants, Heredity (Edinb). 61 (1988) 235–245. https://doi.org/10.1038/hdy.1988.111.

[34] M. Uchida, Y. Aoyama, N. Eda, A. Ohta, Investigation of the Microstructure in the Catalyst Layer and Effects of Both Perfluorosulfonate Ionomer and PTFE-Loaded Carbon on the Catalyst Layer of Polymer Electrolyte Fuel Cells, J. Electrochem. Soc. 142 (1995) 4143–4149. https://doi.org/10.1149/1.2048477.

[35] Y. Utaka, I. Hirose, Y. Tasaki, Characteristics of oxygen diffusivity and water distribution by X-ray radiography in microporous media in alternate porous layers of different wettability for moisture control in gas diffusion layer of PEFC, Int. J. Hydrogen Energy. 36 (2011) 9128–9138. https://doi.org/10.1016/j.ijhydene.2011.04.152.

[36] Park K, Wei Y, So M, Noh TH, Kimura N, Tsuge Y. Influence of Surface Structure on Performance of Inkjet Printed Cathode Catalyst Layers for Polymer Electrolyte Fuel Cells. J Electrochem Energy Convers Storage 2021:1–26. https://doi.org/10.1115/1.4052629.

[37] C.H. Lee, W.J.M. Kort-Kamp, H. Yu, D.A. Cullen, B.M. Patterson, T.A. Arman, S. Komini Babu, R. Mukundan, R.L. Borup, J.S. Spendelow, Grooved electrodes for high-power-density fuel cells, Nat. Energy. 8 (2023) 685–694. https://doi.org/10.1038/s41560-023-01263-2.

[38] T.A. Zawodzinski, C. Derouin, S. Radzinski, R.J. Sherman, V.T. Smith, T.E. Springer, S. Gottesfeld, Water Uptake by and Transport Through Nafion® 117 Membranes, J. Electrochem. Soc. 140 (1993) 1041–1047. https://doi.org/10.1149/1.2056194.

[39] Z. Rajabi, M. Javanbakht, K. Hooshyari, M. Adibi, A. Badiei, Phosphoric acid doped polybenzimidazole based polymer electrolyte membrane and functionalized SBA-15 mesoporous for elevated temperature fuel cell, Int. J. Hydrogen Energy. 46 (2021) 33241–33259. https://doi.org/10.1016/j.ijhydene.2021.07.116.

[40] J. Zhang, S. Chen, H. Bai, S. Lu, Y. Xiang, S.P. Jiang, Effects of phosphotungstic acid on performance of phosphoric acid doped polyethersulfone-polyvinylpyrrolidone membranes for high temperature fuel cells, Int. J. Hydrogen Energy. 46 (2021) 11104–11114. https://doi.org/10.1016/j.ijhydene.2020.07.082.

Table 1.1. Composition and characteristics of various fuel cells

Fuel cell type	Mobile ion	Operating temperature	Application and notes
Alkaline (AFC)	OH^-	50~200 °C	Used in space vehicles, e.g. Apollo, Shuttle.
Proton exchange membrane (PEFC)	H^+	30~100 °C	Vehicles and mobile applications, and for lower power CHP systems.
Direct methanol (DMFC)	H^+	20~90 °C	Suitable for portable electronic systems of low power, running for long times.
Phosphoric acid (PAFC)	H^+	~220 °C	Large numbers of 200-kW CHP systems in use.
Molten carbonate (MCFC)	CO_3^-	~650 °C	Suitable for medium- to large-scale CHP systems, up to MW capacity.
Solid oxide (SOFC)	O^{2-}	500~1000 °C	Suitable for all sizes of CHP systems, 2 kW to multi-MW.

Table 1.2. List of materials used in this study.

Material	**Experiment**	**Simulation**
Catalyst	*Pt/CB (TEC10V50E)	*Pt/CB (TEC10V50E)
Ionomer	Du Pont Nafion solvent 20 %	Proton conductivity assumed to be equivalent to PEM film
PEM	Nafion NRE - 211 (Sigma-Aldrich)	Nafion NRE - 211 (Sigma-Aldrich)
1-propanol	Purity: 99.9%	
Gasket	Si/PEM/Si t=170 μm	
GDL	***SGL25BC (SGLGROUP)	***SGL25BC (SGL GROUP)

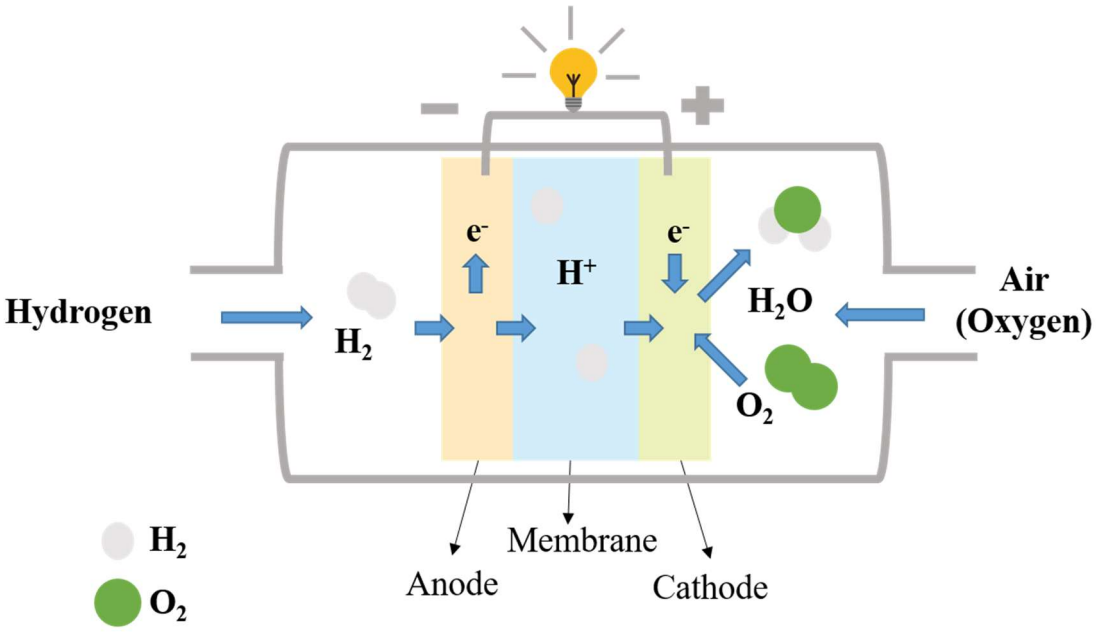

Fig. 1.1. The working principle of fuel cell.

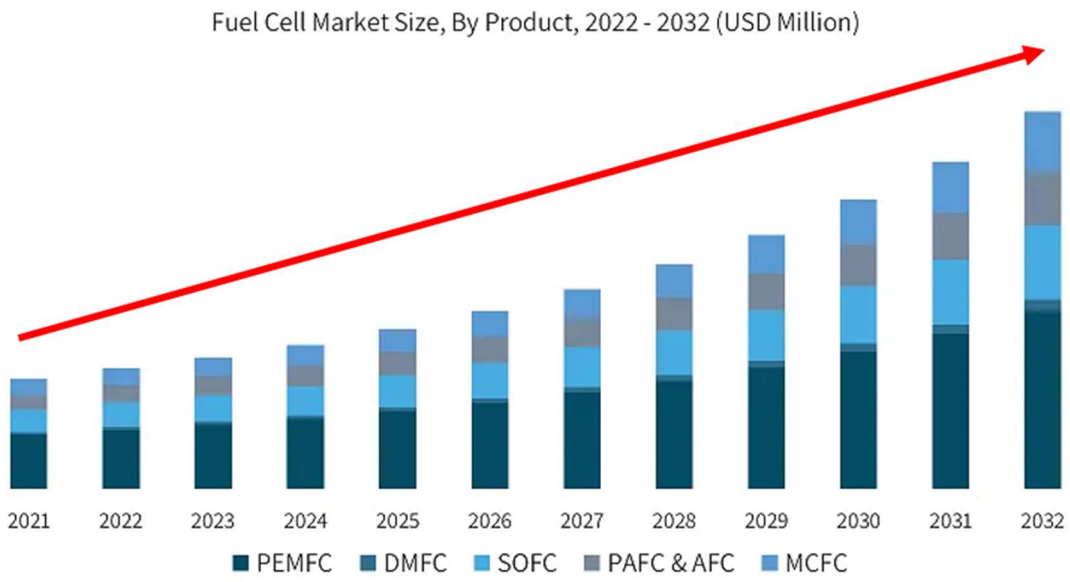

Fig. 1.2. Fuel cell market size, 2022-2032 [7].

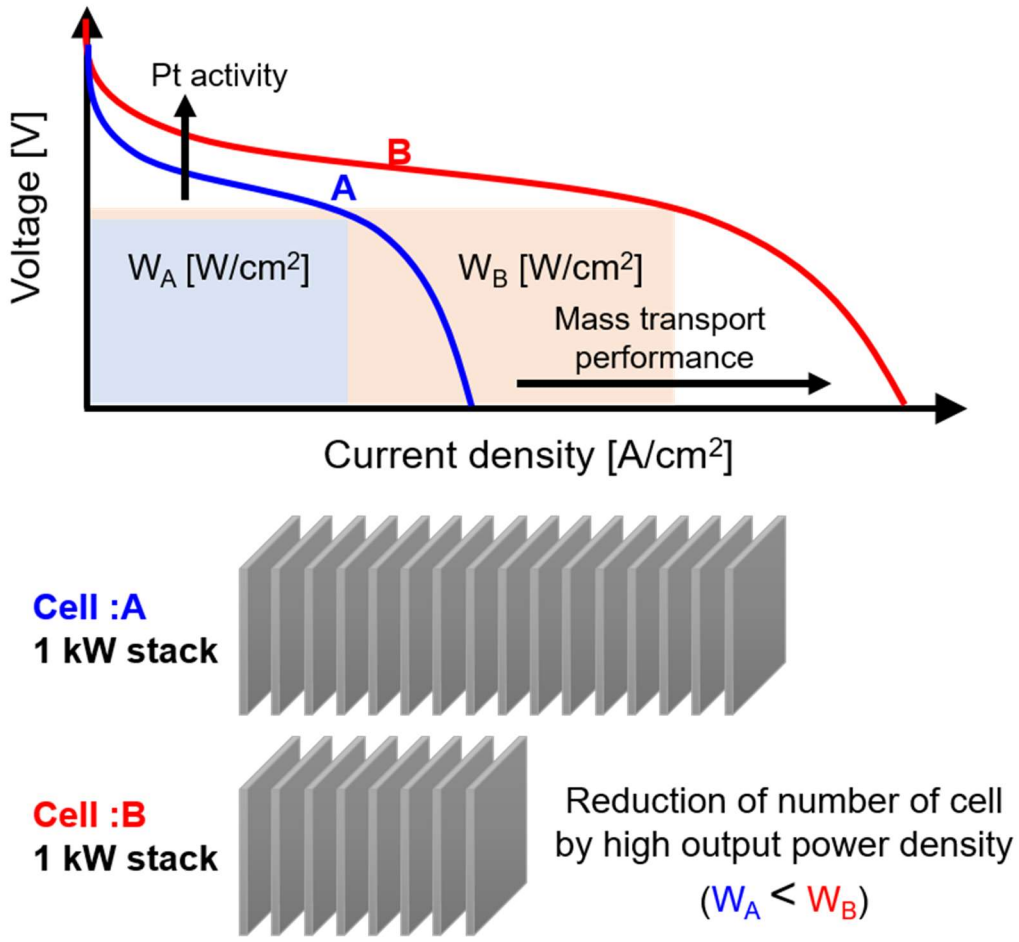

Fig. 1.3. Output power density of PEFC.

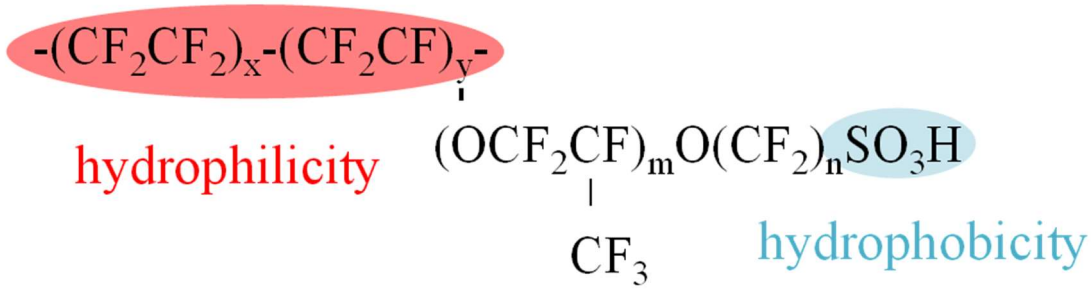

Fig. 1.4. Chemical structure of PFSA (Nafion™).

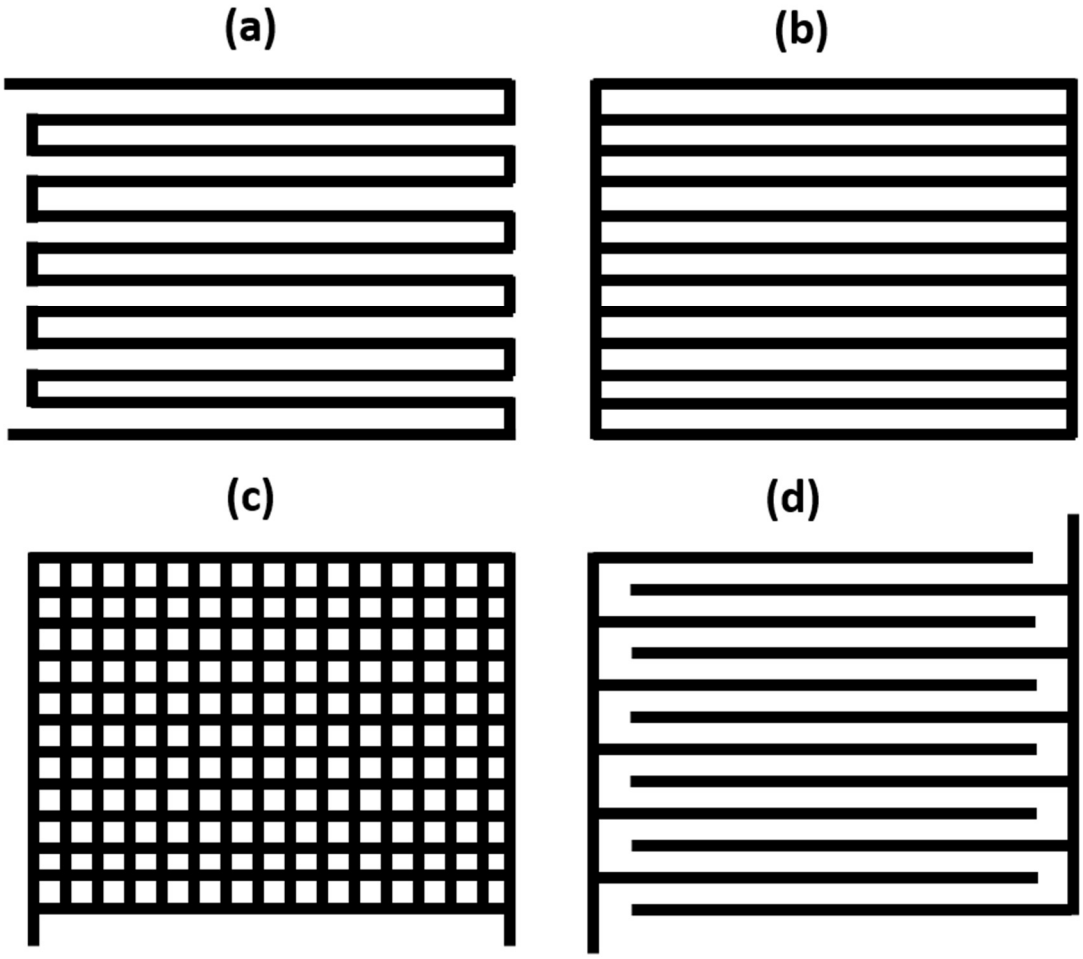

Fig. 1.5. The Schematic of various flow field designs: (a) Serpentine, (b) parallel, (c) interdigitated and (d) mesh (grid, superparallel) as adopted from reference.

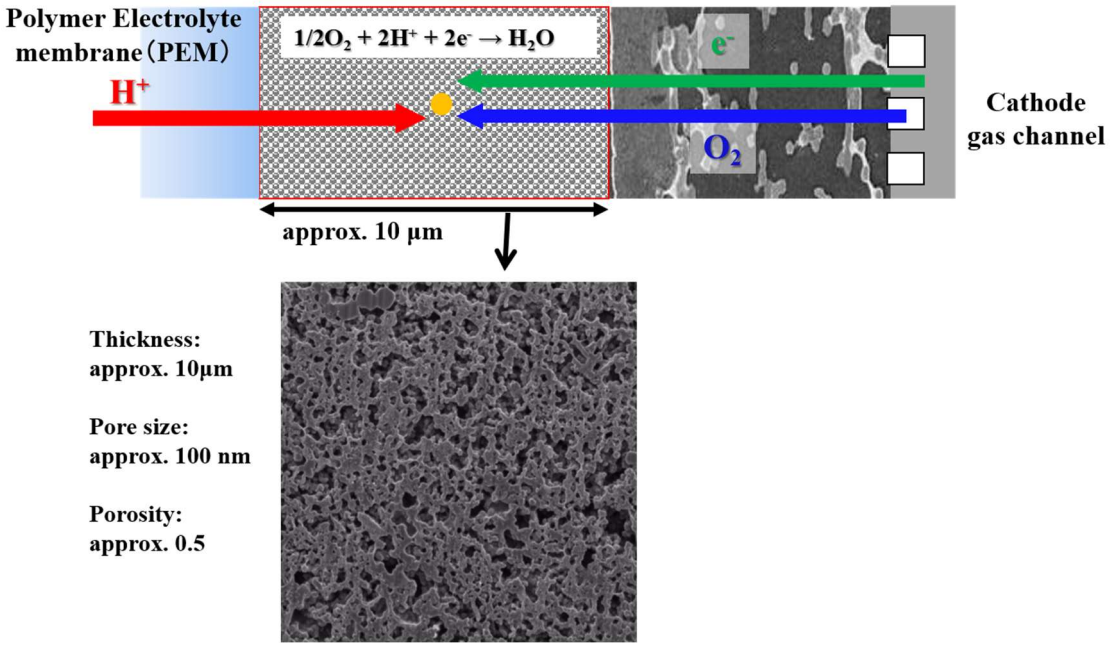

Fig. 1.6. Structure of cathode catalyst layer.

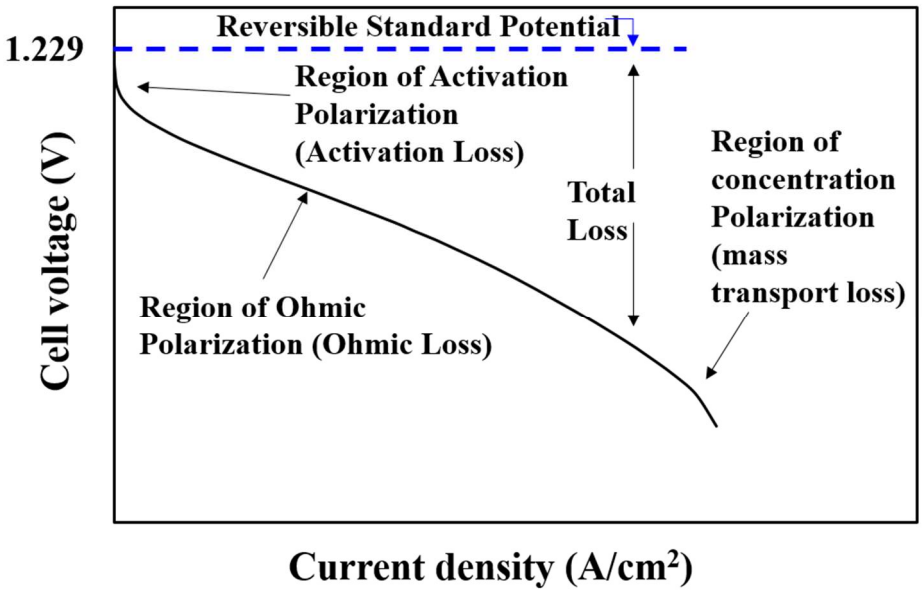

Fig. 1.7. Concept of overvoltage.

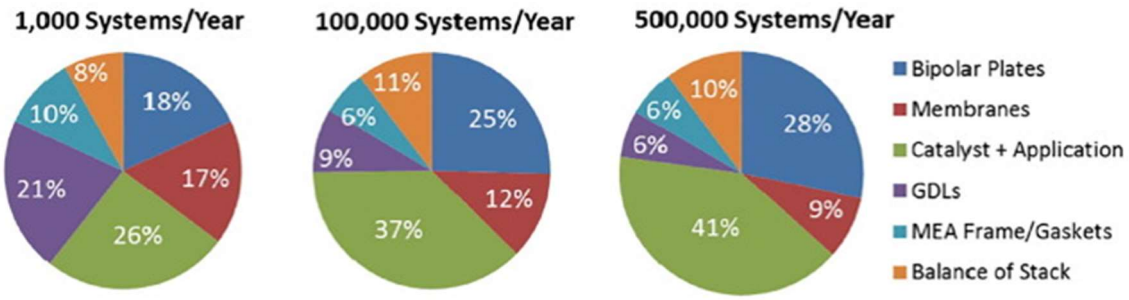

Fig. 1.8. Fuel cell cost breakdown.

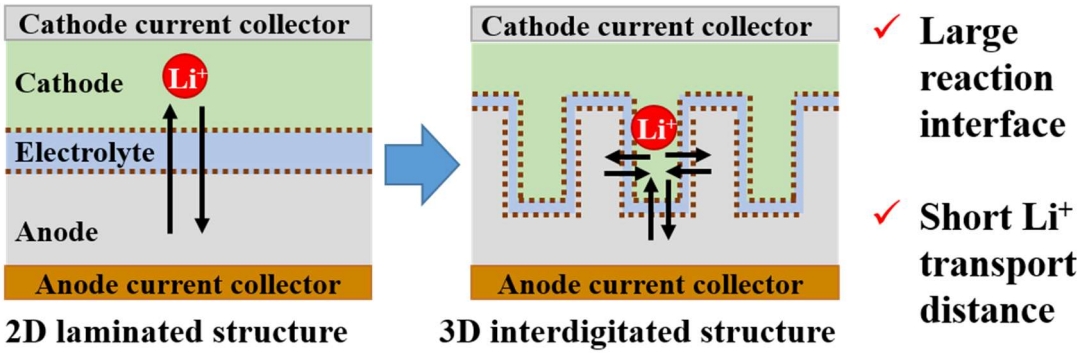

Fig. 1.9. 3D structure applied in Lithium battery.

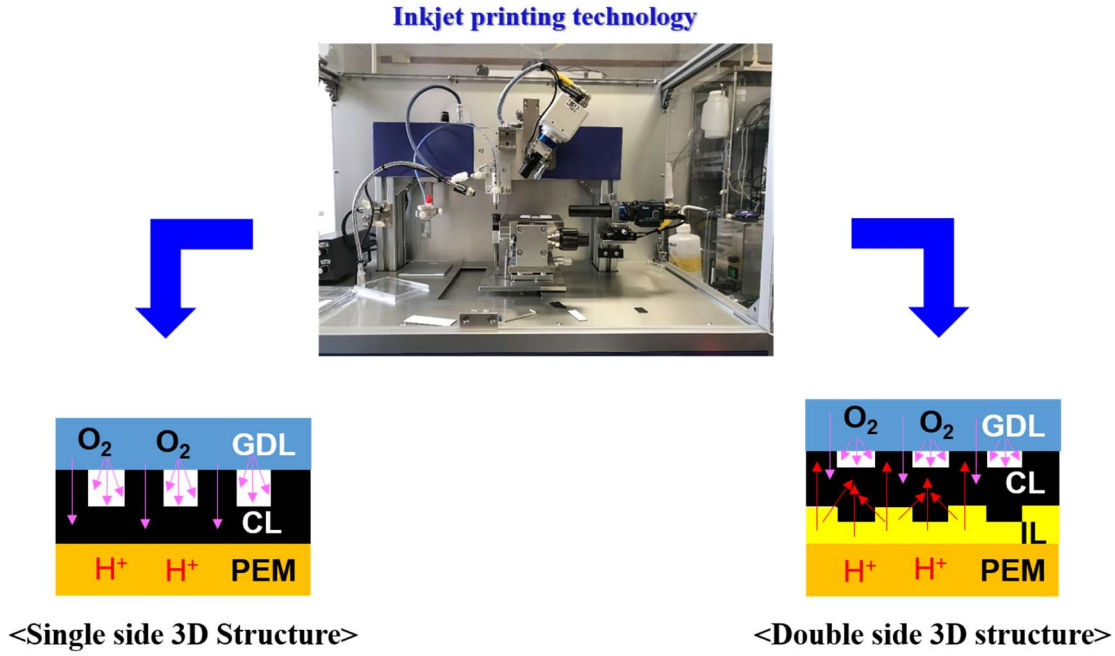

Fig. 1.10. Fabrication of 3D structure of CCL by using inkjet method.

2. Material and Method

2.1 Experiment

2.1.1 Fabrication of Cathode Catalyst Layer and Membrane Electrode Assembly

Catalyst ink for CCLs and carbon-supported Pt catalyst (TEC10V50E; Pt loading: 46.8 %, 0.3 mg/cm^2), purchased from Tanaka Kikinzoku Kogyo, were mixed with distilled water and 1-propanol (NPA). The slurry was dispersed using an ultrasonic homogenizer (Branson Digital sonicator 250DA) for 20 min after the addition of the ionomer (5 wt % Nafion solution, Sigma-Aldrich). The I/C ratio was adjusted to 0.25. In addition, the ionomer solution for the IL was prepared by ultrasonically mixing the ionomer and NPA (ionomer : NPA = 1 : 4) for 5 min. This catalyst ink and ionomer ink was used for fabrication of CCLs. The CCLs were fabricated using the inkjet printing (LaboJet-600STDK, Microjet) method employed in our previous study [1]. Prior to coating the catalyst ink and ionomer ink on the CCLs, a Nafion membrane (NR-211, Chemours) as a PEM and an anode catalyst layer (ACL) were hot-pressed at 413 K and 6 MPa for 4 min. Then, the catalyst ink was printed directly onto the Nafion membrane by the inkjet printing method. In order to use inkjet method, particle size of catalyst is less than 1 μm after dispersion, and it has low viscosity, solvent with high dispersion is used, **Table 2.1** shows the conditions of inkjet printing. Subsequently, the ionomer was also coated using the same method. The real images of the inkjet method are shown in **Fig. 2.1**. The drops pass through the print head and deposit on the Nafion membrane to form the catalyst layer. As shown in **Fig. 2.2**, the image of a single ink drop per layer was captured using a laser microscope to gather basic information for fabricating the catalyst layer structure. From the figure, it is confirmed that as the number of layers increases, the rings remain almost identical but become progressively darker. The ink concentration at the edge is darker than in the interior, as liquid evaporation from the edge is replenished by liquid from the interior, resulting in the coffee ring effect shown in **Fig. 2.3** [2-4]. Typically, researchers avoid this effect when fabricating catalyst layers through inkjet printing. However, in this research, the coffee ring effect was utilized to fabricate a 3D structure for the CCL.

The thickness of the edge and interior is shown in **Fig. 2.4**, confirming that the layer becomes thicker

overall and that the edge is thicker than the interior [1]. Using this coffee ring effect, a 3D structure with a rough catalyst layer surface was fabricated. It was observed that the ink concentration at the edge was darker than in the interior, with liquid evaporation from the edge being replenished by liquid from the interior, resulting in the coffee ring effect. In the flat structure, catalyst ink was immediately dried after printing a drop, allowing the coffee ring effect to help form the 3D structure.

Figure 2.5 shows the procedure for fabricating the catalyst layer and ionomer layer on the PEM. The ink droplets were ejected through the inkjet printer head, and for the 3D pattern, the droplets overlapped as designed after drying the ionomer droplet solution or catalyst inks to maintain their shape. Conversely, a flat pattern was formed by dropping the catalyst ink or ionomer solution until one layer was coated and then drying it to prevent shape formation. Samples were prepared to confirm the structure of each pattern in the IL or CL using the ionomer solution or catalyst ink.

After examining each patterned structure in the IL and CL, CCLs with four structures were fabricated by inkjet printing. The Pt loading of the CCL was 0.3 mg/cm^2, while the I/C ratio was adjusted to 0.25. MEAs with an active area of 1 cm^2 and composed of the anode ACL and CCL on either side of the Nafion film were fabricated. Gas diffusion layers (GDLs; Sigracet25BC, SGL Carbon) containing 5% PTFE and having a thickness of 235 μm were used at both the anode and cathode sides.

2.1.2 Structural Characterization

Figure 2.6 shows the SEM images of the flat- and 3D-patterned structures in each IL and CL at 500 μm (a, b, g, h) and 50 μm (c, d, i, j) scales and the cross-sectional image (e, f, k, l). For the flat-patterned IL (**Fig. 2.6 (a, c)**), no pattern was observed on the surface (a), while the IL surface near the protect film (white color), seen in the upper part of the cross-sectional image (e), had a flat structure. However, it was difficult to distinguish between the Nafion film and the IL surface at the bottom because the material's components are the same as each other. In contrast, for the 3D-patterned IL (shown in **Fig. 2.6 (b,d)**), a rough structural surface was observed in the cross-sectional image (f); the width and height of IL surfaces were about 33 μm and 2.8 μm per each. CLs with two types of patterns coated on the Nafion film are shown in **Fig. 2.6 (g, h, i, j, k, l).** The flat pattern of the CL was observed

(g, i), and the width and height of surfaces was 32.12 μm and 3.76 μm, respectively. This indicates that even if the droplets are continuously printed without drying, the coffee ring effect remains when a pattern is printed using an inkjet printer. Finally, for the 3D-patterned CL, uniform and distinct patterns were observed in the surface images (h, j). The width and height of surfaces was 27.12 μm and 13.63 μm, respectively indicating a rough structure, as evident from the cross-sectional image (l).

In this study, we fabricated CCL structures by combining flat- or 3D-patterned IL or CL. The four types of patterned CCLs investigated in this study are showed in the inset of **Fig 2.7**: (a) Str.1 (ICL W/O+CL 3D), (b) Str.2 (ICL Flat+CL Flat), (c) Str.3 (ICL 3D+CL Flat) and (d) Str.4 (ICL 3D+CL 3D). Str.1 consists only of 3D-patterned CL without IL and was fabricated for comparison because it showed excellent performance in our previous study. Str.2 includes the flat-patterned IL and CL, Str.3 is composed of 3D-patterned IL and flat-patterned CL, and Str.4 is composed of 3D-patterned IL and CL. **Figure 2.7** also presents the SEM image results of the CCLs with various patterned structures. Str.1 is the same as that shown in **Fig. 2.6. (h, j, l)** because only the 3D-patterned CL is included. Str. 2 exhibited a slightly uneven surface, which can be attributed to the 3D-patterned CL, as mentioned in **Fig. 2.6**. The SEM image of Str. 3 showed amorphous heterogeneously agglomerated structures on the flat surface of the CCL. While coating the CL on the IL with the rough surface, particles agglomerated toward the IL surface with the lower height because the catalyst ink droplets are continuously printed without being dried. The height of the amorphous agglomerates, estimated using the digital microscope (VHX-7000), was approximately 9 μm higher than that of the flat surface. Hence, the coat of the flat surface was very thin while that of the amorphous agglomerate was very thick. The pattern of Str. 4 was different from those of Str. 2 and Str. 3. The Str. 4 showed a wider rough pattern than Str. 1 due to the different morphologies of the surfaces of the IL and CL used for fabricating this structure. Thus, CCLs with various structures were successfully fabricated.

2.1.3 PEFC Cell Assembly

To assemble to PEFC cell, the fabricated MEA is sandwiched between a GDL, gasket and separator. **Figure 2.8** shows the real image of GDL, gasket and serpentine. Next, as shown in **Fig. 2.9 (a)**, the

entire cell is bolted, but a gap can be made between the GDL and the catalyst layer if pressure is not uniformly applied and performance evaluation cannot be performed. So, a torque wrench needs to be used to adjust. First, turn the bolt by hand, set the torque wrench to 1 N·m, and tightened 12 bolts. It is tightened in order shown in **Fig. 2.9 (a)**. When finished, the set value is increased in order of 2 N·m and 3 N·m. The single cell is shown in **Fig. 2.9 (b)**. After tightening the cell, the cell was prepared for testing.

2.1.4 Characteristics and Electrochemical Evaluation

Samples were fabricated in order to obtain an information about the electrochemical properties about the various structures.

Figure 2.10 shows the fuel cell testing system. Electrochemical measurements were performed using a single cell (JARI, catalyst area: 10×10 mm^2, serpentine: 1 mm width, 1 mm depth). The aging conditions were as follows: pure H_2 gas and 21 % O_2 with N_2 were humidified and supplied to the anode and cathode, respectively. The conditions of electrochemical evaluation are shown in **Table 2.2**. The aging step was conducted by cycling the potential between the OCV and 0.3 V for 30 s until the current remained constant at 0.3 V. In order to stabilize the performance of the membrane, aging of the catalyst layer which continues to apply the load with a constant current before it is used in the experiment is necessary. The I-V curves were measured from 0.9 to 0.2 V in decrements of 0.1 V. The respective potentials were maintained for 5 min until the current stabilized at this point, the gas flow rates were 250 and 500 mL/min at the anode and cathode, respectively, the temperatures were 80 °C, the relative humidity (RH) values were 100 % and 40 % and oxygen concentration were 21 % and 10 %. Also electrochemical impedance spectra (EIS) was performed over a frequency of 100 kHz. And then we took that sample to observe through laser microscope (OLS4500, Olympus).

2.2 Theoretical Estimation

In a previous study [1], CLs with flat or 3D structures were theoretically analyzed. In this study, the IL of the proton channel was structured, and a theoretical equation was used to understand the effect

of the 3D patterned structure. We converted the oxygen-related equations into the proton-related equations. In the previous study [1], the Butler-Volmer equation r_{O_2} was converted into a first-order reaction in relation to oxygen pore concentration, $C_{O_2}^{(pore)}$, with the assumption that the reaction was isothermal and limited by the oxygen diffusion in the CCL as follows:

$$r_{O_2} = a_{Pt}^{eff} \frac{1}{4F} \frac{i_0^{ref}}{C_{O_2}^{ref}} \exp\left(\frac{n\alpha_c F}{RT} \eta_{local} \right) \frac{RT}{H} C_{O_2}^{(pore)}, \quad (2.1)$$

where i_{Pt} is the current density on the Pt surface, F is Faraday's constant, i_0^{ref} is the reference exchange current density, $C_{O_2}^{ref}$ is the reference oxygen concentration, a_{Pt}^{eff} is the effective Pt surface area per local volume, n is the- number of electrons, α_c is the charge transfer coefficient, R is the gas constant, T is the temperature, η is the local overvoltage, and H is Henry's coefficient. The first order reaction coefficient of oxygen, k_{O_2}, is given by:

$$k_{O_2} = a_{Pt}^{eff} \frac{1}{4F} \frac{i_0^{ref}}{C_{O_2}^{ref}} \exp\left(\frac{n\alpha_c F}{RT} \eta \right) \frac{RT}{H}, \quad (2.2)$$

which will be introduced to Thiele modulus's equation. Thiele modulus is the ratio of the rate of reaction to the rate of diffusion of a reactant. When the coefficient is large, the reaction rate is controlled by diffusion, and the kinetically controlled reaction becomes insignificant. When the coefficient is small, the reaction rate is kinetically controlled, and the diffusion-controlled reaction is insignificant [5]. Herein, the Thiele modulus was used to estimate the effectiveness factor of the CCLs. The Thiele modulus is a dimensionless quantity and can be expressed in terms of k_{O_2} and L_D, as follows:

$$\phi = L_{\mathrm{D}} \sqrt{\frac{k_{\mathrm{O_2}}}{D_{\mathrm{O_2}}^{\mathrm{eff}}}} \tag{2.3}$$

Next, Thiele modulus and diffusion length were introduced to explain the effect of CL structures in **Fig 2.11** on the cell performance. The diffusion lengths of the reactant on the CCLs (L_{D}) were calculated using the following equation:

$$L_{\mathrm{D}} = \frac{w_{\mathrm{s}}}{w_{\mathrm{s}} + h_{\mathrm{s}}} h_{\mathrm{CL}} \tag{2.4}$$

Here, w_{s} is the gap width, h_{s} is the gap height, and h_{CL} is the thickness of the catalyst layer as shown in **Fig. 2.11 (a)**. The effective oxygen diffusion coefficient, $D_{\mathrm{O_2}}^{\mathrm{eff}}$ was calculated using the following relation with porosity, ε, according to Inoue *et al*. [6]:

$$D_{\mathrm{O_2}}^{\mathrm{eff}} = D_{\mathrm{O_2}} \varepsilon^{6} . \tag{2.5}$$

Here, $D_{\mathrm{O_2}}$ is the bulk oxygen diffusion coefficient. As mentioned above, the Thiele modulus was used to estimate the effectiveness factor of the CLs. An effectiveness factor in the range of 0-1 for isothermal conditions indicates the importance of diffusion and kinetic limitations and can also be considered as the amount of reactants that penetrates the CL [7]. The effectiveness factor (β) is expressed as follows:

$$\beta = \frac{\tanh \phi}{\phi}, \tag{2.6}$$

which is plotted in **Fig. 2.11 (c).** Further, new structures of IL was investigated as shown in **Fig. 2.11 (b).** To relate the Butler-Volmer equation to proton conduction in these structures, i was expressed by assuming that the reaction was isothermal and limited by proton conductivity in the IL as follows [7]:

$$i = i_o \left[\exp\left(\frac{(1-\alpha_c)Fn}{RT}\eta \right) - \exp\left(\frac{-\alpha_c Fn}{RT}\eta \right) \right] \tag{2.7}$$

where the exchange current density, i_0, is given by

$$i_0 = i_0^{(\mathrm{ref})} \frac{C_{\mathrm{O_2}}^{(\mathrm{pore})}}{C^{\mathrm{ref}}} \frac{RT}{H} \tag{2.8}$$

The purpose of this study is to coat the IL, which is the path for the proton, for in order to improve the proton conductivity. Thus, we consider the equations related to protons. Expressing **Eq. 2.7** as the first order Taylor equation, $\exp(x) \approx 1 + x$, we have,

$$i = i_0 \left[\left(1 + \frac{(1-\alpha_c)Fn}{RT}\eta \right) - \left(1 + \frac{-\alpha_c Fn}{RT}\eta \right) \right] \tag{2.9}$$

which can be simplified as follows:

$$i = \frac{nFi_0}{RT}\eta \tag{2.10}$$

$$\eta = E + \Phi_{\mathrm{H^+}} - \Phi_{e^-} \tag{2.11}$$

where E is the equilibrium potential, $\Phi_{\mathrm{H^+}}$ is proton potential, Φ_{e^-} is electron potential. Further, we assumed that the reaction was limited by the proton conduction in the CCL while E and Φ_{e^-} were constant. Hence, the Butler-Volmer equation (**Eq. 2.9**) was converted into a first-order reaction r_{H^+} (mol m^{-3} s^{-1}) in respect to η by introducing **Eq. 2.12** as follows:

$$r_{H^+} = \frac{a_{\mathrm{Pt}} i}{F} \approx a_{\mathrm{Pt}} \frac{ni_0}{RT}\eta = k_{\mathrm{H^+}}\eta \tag{2.12}$$

Here, $k_{\mathrm{H^+}}$ (mol m^{-3} s^{-1} V^{-1}) is the first-order reaction coefficient in respect to η given as follows:

$$k_{\mathrm{H^+}} = a_{\mathrm{Pt}} \frac{ni_0}{RT} \tag{2.13}$$

In case of IL related to proton, the Thiele modulus also could be used to estimate the effectiveness factor of the CCLs. The Thiele modulus is a dimensionless quantity and can be expressed in terms of $k_{\mathrm{H^+}}$ and L_{C}, as follows:

$$\phi = L_{\mathrm{C}} \sqrt{\frac{Fk_{\mathrm{H^+}}}{\sigma_{\mathrm{H^+}}^{\mathrm{eff}}}} = L_{\mathrm{C}} \sqrt{\frac{Fa_{\mathrm{Pt}} ni_0}{RT\sigma_{\mathrm{H^+}}^{\mathrm{eff}}}} \tag{2.14}$$

Next, this Thiele modulus and conduction length was introduced to explain the effect of CL on the cell performance. The conduction lengths of the reactant on the CCLs (L_c) were calculated in the same way as that of the diffusion limitation as follows:

$$L_C = L_D = \frac{w_{\mathrm{s}}}{w_{\mathrm{s}} + h_{\mathrm{s}}} h_{\mathrm{CL}} . \tag{2.15}$$

$\sigma_{\mathrm{H^+}}^{\mathrm{eff}}$ is the effective proton conductivity expressed as following equation from the literature [8]:

$$\sigma_{\mathrm{H^+}}^{\mathrm{eff}} = \sigma_{\mathrm{H^+}}^{\mathrm{ionomer}} (R_{I/C})^{1.8} (V_{CB})^2 \tag{2.16}$$

where $\sigma_{\mathrm{H^+}}^{\mathrm{ionomer}}$ is the bulk proton conductivity of ionomer, $R_{I/C}$ is the ionomer and carbon weight ratio and V_{CB} is the volume ratio of the carbon black.

In **Fig. 2.11 (a)**, CL with a 3D structure has a larger contact surface area with oxygen than that of a flat structure. When these structures were calculated by the diffusion length of reactants expressed in **Eq. 2.5**, the diffusion length at the CL with 3D structure is shorter than that of the flat structure. When calculated by applying the diffusion length of these structures to the Thiele modulus of **Eq. 2.6**, the value of Thiele modulus is higher as the diffusion length is longer. Thus, the value of the CL with 3D

structure is smaller than that of the flat structure. As a result, in the graph of the relationship between the effectiveness factor and Thiele modulus shown in **Fig. 2.11 (c)**, it can be seen that the effectiveness factor of CL with 3D structure has a value higher than that of CL with flat. This indicates that the 3D structure can affect the improvement of cell performance. On the other hand, IL with 3D structure for shortening the proton conduction path and improving proton conductivity can be calculated as Thiele modulus expressed in **Eq. 2.14**. In **Fig. 2.11 (b)**, CL also has a 3D structure in the boundary structure between CL and IL with the 3D structure. Even if IL exists, the effectiveness factor is dependent on the 3D structure of CL because IL is not the place to occur the reaction. Thus, as the structure of CL changes, it corresponds to the effect of CL with the 3D structure on the cell.

2.3 Boundary Conditions

An overview of the boundary conditions for the oxygen, proton and electron mass/charge transport through the MEA are shown in **Fig 2.11.** The main resistances occur in GDL, CCL and PEM, while the resistances in ACL were ignored.

2.3.1 Oxygen Concentration in Catalyst Layer Void

The oxygen concentration at the inlet of the separator channel $C_{O_2}^{(\text{channel})}$ was set to a reference value. The oxygen concentration at the GDL/CCL interface was calculated from the separator channel as a flux constant in the oxygen diffusion process in the GDL as follows:

$$C_{O_2}^{(\text{CCL/PEM})} = C_{O_2}^{(\text{channel})} - \frac{i}{4F} \frac{l_{\text{GDL}}}{D_{O_2} \frac{\varepsilon_{\text{GDL}}}{\tau_{\text{GDL}}}} \tag{2.17}$$

At the CCL/PEM interface, no oxygen flux boundary conditions were applied which resulted in a local zero oxygen gradient.

2.3.2 Water Vapor Concentration in Catalyst Layer Void

The water vapor concentration at the PEM/CL interface is given by the amount of current reaction at the PEM/CL interface. The water vapor concentration at the GDL/CCL interface was calculated from the separator channel as a flux diffusion process in the GDL. The calculation formula is as follows:

$$C_{H_2O}^{(CL/GDL)} = C_{H_2O}^{(channel)} - \frac{i}{4F}\frac{l_{GDL}}{D_{H_2O}\frac{\varepsilon_{GDL}}{\tau_{GDL}}} \tag{2.18}$$

At the CCL/PEM interface, no oxygen flux boundary conditions were applied similarly to that of the oxygen calculations.

2.3.3 Electrolyte, Proton in Carrier and Electron Potential of CCL

An overview of the overpotentials in the MEA is depicted in **Fig 2.12.** The definition of overpotential on the anode and cathode side is as follows:

$$\text{Anode side: } \eta_{HOR} = \Phi_C^a - \Phi_M^a + U_{HOR} \tag{2.19}$$

$$\text{Cathode side: } \eta_{ORR} = \Phi_M^c - \Phi_C^c + U_{ORR} \tag{2.20}$$

Where η is the overvoltage of the electrode reaction, Φ_e is electron potential, Φ_p is proton potential, a means anode, c means cathode, HOR is hydrogen oxidation reaction and ORR is oxygen reduction reaction [8-12]. From both formulas:

$$\eta_{HOR} + \eta_{OER} = \Phi_e^a - \Phi_e^c - \Phi_p^a + \Phi_p^c + U_{HOR} + U_{ORR} \tag{2.21}$$

$$\Phi_e^c - \Phi_e^a = U_{HOR} + U_{ORR} - \eta_{HOR} - \eta_{OER} - (\Phi_p^a - \Phi_p^c) \tag{2.22}$$

Where electron potential difference between the anode and cathode is cell voltage. Since the proton potential difference between the anode and cathode is a loss overvoltage due to membrane resistance, it can be expressed as follows:

$$V = E - \eta_{\mathrm{HOR}} - \eta_{\mathrm{OER}} - \eta_{\mathrm{mem}} \tag{2.23}$$

$$V = \Phi_{\mathrm{e}}^{\mathrm{c}} - \Phi_{\mathrm{e}}^{\mathrm{a}}\ , \quad E = U_{\mathrm{HOR}} + U_{\mathrm{ORR}}\ , \quad \eta_{\mathrm{mem}} = \Phi_{\mathrm{p}}^{\mathrm{a}} - \Phi_{\mathrm{p}}^{\mathrm{c}} \tag{2.24}$$

Further, the electron potential at the CCL/GDL interface and the proton potential at the CCL/PEM interface are as follows:

$$\Phi_{\mathrm{e}}^{\mathrm{c}} = V \quad \text{at CL/GDL interface} \tag{2.25}$$

$$\Phi_{\mathrm{p}}^{\mathrm{c}} = -\eta_{\mathrm{mem}} \quad \text{at interface CL PEM} \tag{2.26}$$

2.3.4 Oxygen Concentration and Proton Potential Around Carrier

The conversion from pore concentration to the concentration in the ionomer follows Henry's law while the proton potential is kept as the value in the electrolyte as follows:

$$C_{\mathrm{O_2}}^{(\mathrm{surf})} = C_{\mathrm{O_2}}^{(\mathrm{void})} \frac{RT}{H} \tag{2.27}$$

$$\Phi_{\mathrm{p}}^{(\mathrm{surf})} = \Phi_{\mathrm{p}}^{\mathrm{c}} \tag{2.28}$$

2.4 Numerical Model

2.4.1 Calculation Assumptions

In this study, the following calculation assumptions were assumed.

1. There is no temperature gradients or temporal changes inside the fuel cell.
2. The steady state inside CL is considered.
3. The effect of diffusion of water vapor in CL voids on oxygen diffusion can be ignored.
4. Anode reactions can be ignored (anode charge/mass transport do not limit reaction).
5. Effects of carbon corrosion and Pt dissolution can be ignored.
6. The carbon carrier is filled with generated water, and oxygen and protons can easily be transferred.
7. Dissolution resistance at water boundary generated in ionomer and carrier pores is ignored.
8. Since the transport resistance of electrons in the carbon black carrier is considered to be very small compared to the transport resistance of proton oxygen, the potential distribution in the carrier is uniform.
9. Proton conductivity of ionomer is equivalent to that of the PEM.

2.4.2 Simulation Method of Overvoltage Separation

Overvoltage is the difference between the theoretical potential of the reaction and the cell voltage when the actual reaction progresses, and corresponds to the voltage loss that could not be taken out as power. It is believed that the factors of internal resistance are greatly separated by the transport resistance and reaction resistance of the reacting material, and it is considered to be lost due to the resistance inside the fuel cell.

To quantitatively compare the resistance and reaction resistance components of oxygen, proton, and electron transport, which are reacting substances of cathode reactions, to understand the speed-dominating stage, as shown in **Fig. 2.12**, overvoltage separation was performed, and the average value of various overvoltages was simulated. Overvoltage η_{all} is total reaction overvoltage which includes activation overvoltage $\eta_{(\mathrm{act})}$, reaction overvoltage due to platinum oxide formation η_{PtOx}, proton transport overvoltage in PEM $\eta_{\mathrm{p}}^{(\mathrm{mem.})}$, proton transport overvoltage in the ionomer part in the CCL

$\eta_{\mathrm{p}}^{(\mathrm{ion.})}$, electron transport overvoltage in the CCL $\eta_{\mathrm{e}}^{(\mathrm{sup.})}$, oxygen transport overvoltage to GDL/CL boundary position $\eta_{\mathrm{O_2}}^{\mathrm{GDL}}$, oxygen transport overvoltage in the void part of the CCL $\eta_{\mathrm{O_2}}^{\mathrm{CL}}$, oxygen dissolution overvoltage to ionomer $\eta_{.\mathrm{O_2}}^{\mathrm{diss.\,ion}}$, oxygen transport overvoltage in the ionomer part $\eta_{\mathrm{O_2}}^{\mathrm{dif.\,ion.}}$, oxygen transport overvoltage inside the carrier pores $\eta_{\mathrm{O_2}}^{\mathrm{dif.\,pore}}$ can be separated into 10 overvoltages, and can be expressed as follows.

$$\eta_{\mathrm{all}} = \eta_{\mathrm{act.}} + \eta_{\mathrm{PtOx}} + \eta_{\mathrm{p}}^{\mathrm{mem.}} + \eta_{\mathrm{p}}^{\mathrm{ion.}} + \eta_{\mathrm{e}}^{\mathrm{sup.}} + \eta_{.\mathrm{O_2}}^{\mathrm{chan}} + \eta_{\mathrm{O_2}}^{\mathrm{CL}} + \eta_{\mathrm{O_2}}^{\mathrm{diss.\,ion.}} + \eta_{\mathrm{O_2}}^{\mathrm{dif.\,ion.}} + \eta_{\mathrm{O_2}}^{\mathrm{dif.\,pore}} \tag{2.29}$$

Each overvoltage will be explained how to calculate. The overvoltage of cathode side can be expressed by the following equation:

$$\eta_{\mathrm{ORR}} = \Phi_{\mathrm{p}}^{\mathrm{c}} - \Phi_{\mathrm{e}}^{\mathrm{c}} + U_{\mathrm{ORR}} \tag{2.30}$$

The possible overvoltage of the CCL is expressed below:

$$\text{Proton conductive overvoltage:} \quad \Phi_{\mathrm{p}}^{\mathrm{c}} = -\eta_{\mathrm{p}}^{\mathrm{mem}} - \eta_{\mathrm{p}}^{\mathrm{ion.}} \tag{2.31}$$

$$\text{Electron conductive overvoltage:} \quad \Phi_{\mathrm{e}}^{\mathrm{c}} = V + \eta_{\mathrm{e}}^{\mathrm{sup.}} \tag{2.32}$$

The resistance overvoltage of the membrane $\eta_{\mathrm{p}}^{\mathrm{mem}}$ is simulated from the proton conductivity and the set current density of the membrane. Here, the Butler-Volmer equation is arranged into an overvoltage, and the following equation is obtained when the logarithmic of two-side number is taken:

$$\eta \ = \eta_{\mathrm{act.}} + \eta_{\mathrm{O_2}}^{\mathrm{con.}} = \frac{RT}{n\alpha F}\ln\frac{i}{i_0^{\mathrm{eff}}} + \frac{RT}{n\alpha F}\ln\frac{1}{f} + \frac{RT}{n\alpha F}\ln\frac{C_{\mathrm{O_2}}^{\mathrm{ref}}}{C_{\mathrm{O_2}}}. \tag{2.33}$$

Here, the terms on apparent oxygen exchange current density and platinum oxidation are summarized as follows.

$$i_0^{\text{eff}} = i_0^{\text{ref}} a_{\text{Pt}} \tag{2.34}$$

$$f = \left(1 - \theta_{\text{PtOX}}\right) \exp\left(-\frac{\omega \theta_{\text{PtOx}}}{RT}\right) \tag{2.35}$$

The above equations show each factor for overvoltage, and by calculating these overvoltages, it is possible to compare the ratio of each factor to the total overvoltage. In addition, because the overvoltage is calculated for each local potential, a distribution is observed in the overvoltage. However, but in this study, each overvoltage was compared according to the value taken by the arithmetic average.

2.4.3 Simulation Procedure and Parameter

The procedure of this simulation is shown in **Fig. 2.13**, First, the carbon black agglomeration structure is digitized based on statistics on the primary size and number of particles, the conditions of simulating carbon black are shown in **Table 2.3**. Next, carbon black packing structure (1 μm^3) with ionomer was simulated as microscale heterogeneous structure of CCL, the conditions of simulating CCL in micro-scale are shown in **Table 2.4.** Finally, a macroscale 3D CCL structure was modeled by stacking a microscale structure; the conditions of simulating the macroscale CCL are shown in **Table 2.5**. The size was adjusted to actual experimental structure.

As mentioned before, this simulation used block method for the calculations, and the mesh size was 2 nm, the block size was 200 nm, from the **Fig. 2.14**. For the assumption in the calculations, the CL was assumed to have homogeneous temperature distribution, water was assumed to be entirely in water vapor condition, and the humidity was 100%, and the pressure was set to atmospheric pressure.

2.5. Cathode Catalyst Layer Configuration in Simulation

As reported in previous papers [6,13], additional ILs using 3D-pattern CLs can improve cell performance. This structure increases cell performance by adding ILs related to proton conductivity within CLs to increase proton conductivity toward CLs. To proceed with the simulation for these structures, the basic unit blocks of CCLs and ILs were simulated with CCLs 3D-pattern structures to easily and simultaneously reconstruct the 3D-pattern structural shapes of CCLs. Because the optimal structure to increase proton conductivity under the same conditions should be found, this study classified the structure into five types and set other conditions by changing the position and size of the ILs while the volume of the ILs remains constant. Details are shown in **Fig. 2.15.** The 3D structure consists of 100 x 100 x 100 nm blocks of CCLs. Next, the CCLs and ILs block stacks were 3D between PEMs and GDLs, and were classified into various types of structures including conventional flat structures and 3D-pattern structures were simulated [14]. Furthermore, the optimization for IL was performed by constructing different aspect ratio (AR) of IL in CCL, as shown in **Fig. 2.16**.

Nomenclature

a_{Pt}	Pt surface area per local volume ($m^2 \cdot m^{-3}$)
$C_{\mathrm{O_2}}^{(\mathrm{pore})}$	Oxygen concentration in the local pore space ($mol \cdot m^{-3}$)
$C_{\mathrm{O_2}}^{(\mathrm{channel})}$	Gas channel oxygen concentration ($mol \cdot m^{-3}$)
$C_{\mathrm{O_2}}^{\mathrm{ref}}$	Reference oxygen concentration ($mol \cdot m^{-3}$)
$D_{\mathrm{O_2}}$	Bulk oxygen diffusion coefficient ($m^2 \cdot s^{-1}$)
$D_{\mathrm{O_2}}^{\mathrm{eff}}$	Effective oxygen diffusion coefficient ($m^2 \cdot s^{-1}$)
F	Faraday's constant ($C \cdot mol^{-1}$)
H	Henry's coefficient ($J \cdot mol^{-1}$)
h_{CL}	Thickness of catalyst layer (m)

h_s	Gap height (m)
i_0^{ref}	Exchange current density ($A \cdot m^{-2}$)
i_{Pt}	Current density on the Pt surface ($A \cdot m^{-2}$)
k_{H^+}	First order reaction coefficient of proton potential ($mol\ m^{-3}\ s^{-1}\ V^{-1}$)
k_{O_2}	First order reaction coefficient of oxygen (s^{-1})
L_D	Reactant diffusion lengths of the CCLs (m)
n	The number of electrons (-)
R	Gas constant ($J \cdot K^{-1} \cdot mol^{-1}$)
r_{H^+}	Proton reaction rate ($mol \cdot m^{-3} \cdot s^{-1}$)
r_{O_2}	Oxygen reaction rate ($mol \cdot m^{-3} \cdot s^{-1}$)
T	Temperature (K)
w_s	Gap width (m)
α_c	Charge transfer coefficient (-)
β	Effectiveness factor (-)
ε	Porosity (-)
η_{local}	Local overvoltage (V)
ϕ	Thiele modulus (-)
Φ_{e}	Electron potential (V)
Φ_{p}	Proton potential (V)

References:

[1] Park K, Wei Y, So M, Noh TH, Kimura N, Tsuge Y. Influence of Surface Structure on Performance of Inkjet Printed Cathode Catalyst Layers for Polymer Electrolyte Fuel Cells. J Electrochem Energy Convers Storage 2021:1–26. https://doi.org/10.1115/1.4052629.

[2] Deegan RD, Bakajin O, Dupont TF, Huber G, Nagel SR, Witten TA. Capillary flow as the cause of ring stains from dried liquid drops. Nature (1997);389:827–9. https://doi.org/10.1038/39827.

[3] Choi S, Stassi S, Pisano AP, Zohdi TI. Coffee-ring effect-based three dimensional patterning of micro/nanoparticle assembly with a single droplet. Langmuir (2010);26:11690–8. https://doi.org/10.1021/la101110t.

[4] Yunker PJ, Still T, Lohr MA, Yodh AG. Suppression of the coffee-ring effect by shape-dependent capillary interactions. Nature (2011);476:308–11. https://doi.org/10.1038/nature10344.

[5] Allen J.BARD, Larry R. FAULKNER "Electrochemical methods fundamentals and applications second edition".

[6] Inoue G, Ohnishi T, So M, Park K, Ono M, Tsuge Y. Simulation of carbon black aggregate and evaluation of ionomer structure on carbon in catalyst layer of polymer electrolyte fuel cell. J Power Sources 2019;439:227060. https://doi.org/10.1016/j.jpowsour.2019.227060.

[7] O'Neil K, Meyers JP, Darling RM, Perry ML. Oxygen gain analysis for proton exchange membrane fuel cells. Int J Hydrogen Energy 2012;37:373–82. https://doi.org/10.1016/j.ijhydene.2011.08.085.

[8] Ohma A, Ichiya T, Fushinobu K, Okazaki K. Oxygen Reduction Reaction Paths and Behavior of Hydrogen Peroxide Formation on Pt (111) for PEMFC. ECS Meet Abstr 2009;MA2009-02:873–873. https://doi.org/10.1149/ma

[9] A. Ishihara, Y. Shibata, S. Mitsushima, K. Ota, Partially Oxidized Tantalum Carbonitrides as a New Nonplatinum Cathode for PEFC–1–, J. Electrochem. Soc. 155 (2008) B400. https://doi.org/10.1149/1.2839606.

[10] N.P. Subramanian, T.A. Greszler, J. Zhang, W. Gu, R. Makharia, Pt-Oxide Coverage-Dependent Oxygen Reduction Reaction (ORR) Kinetics, J. Electrochem. Soc. 159 (2012) B531–B540. https://doi.org/10.1149/2.088205jes.

[11] S. Jomori, N. Nonoyama, T. Yoshida, Analysis and modeling of PEMFC degradation: Effect on oxygen transport, J. Power Sources. 215 (2012) 18–27. https://doi.org/10.1016/j.jpowsour.2012.04.069.

[12] K.C. Neyerlin, W. Gu, J. Jorne, A. Clark, H.A. Gasteiger, Cathode Catalyst Utilization for the ORR in a PEMFC, J. Electrochem. Soc. 154 (2007) B279. https://doi.org/10.1149/1.2400626.

[13] G. Inoue, M. Kawase, Effect of porous structure of catalyst layer on effective oxygen diffusion coefficient in polymer electrolyte fuel cell, J. Power Sources. 327 (2016) 1–10. https://doi.org/10.1016/j.jpowsour.2016.07.037.

[14] K. Park, M. So, M. Goto, S. Takenaka, Y. Tsuge, G. Inoue, Numerical analysis of silica coating effect on Pt cathode catalyst in polymer electrolyte fuel cells, J. Chem. Eng. Japan. 54 (2021) 226–231. https://doi.org/10.1252/jcej.20we102.

Table 2.1 Conditions of inkjet method.

Type	Value	Units
Catalyst	TEC10V50E	[-]
Ionomer/carbon	0.25	[-]
Solution concentration	2	[wt %]
Drop a peed	6.5~7.0	[m/s]
Pitch/width	32 or 125	[μm]
Head voltage	28	[V]
1^{st} pulse width	70	[μs]

Table 2.2 Conditions of electrochemical evaluation.

	Current density or voltage	Flow		Cell temperature	Inlet temperature	Humidification & gas phase	
		H_2 Ncc/min	Air Ncc/min			H_2	Air
	(A/cm^2 or mA/s or V)			℃	℃	℃	℃
Aging	OCV-0.3V(60s)	1000	N_2 1580 O_2 420	40	100	55	55
Purge	OCV	1000	N_2 1000	80	90	79	79
Limiting current	0.9V~0.1V(100mV/s)*1 0.9V~0.1V(10mV/s)*3	1000	N_2 1000 Air 52	80	90	79	79
Purge	OCV	1000	N_2 1000	80	90	80	80
X over current	0.1V~0.9V(100mV/s)(CV) 0.2V~0.5V(1mV/s)(LSV)	1000	N_2 1000	80	90	80	80
Purge	OCV	250	N_2 0	80	90	80	80
ESCA	0.02V~0.9V(50mV/s)	250	N_2 0	80	90	80	80
Purge	OCV	250	N_2 395 O_2 105	80	90	80	80
ORR	0.09V~1.0V(50mV/s)	250	N_2 395 O_2 105	80	90	80	80
i-V	0.9V~0.2V (measure impedance of each voltage)	250	N_2 395 O_2 105	80	90	80	80

Table 2.3. Conditions of simulating carbon black.

Properties	Value	Units
Particle distribution	30	[nm]
Number of types of structures to be produced	100	[-]
Numbers of particles	25	[-]
Structure	Branch type	[-]
Mesh size	2.0	[nm]

Table 2.4. Conditions of simulating CCL (micro-scale).

Property	Value	Units
Catalyst layer dimensions	1.0×1.0×1.0	[μm]
Structure type	Branch type	[-]
Pt loading type	Random	[-]
Ionomer type	Uniform code	[-]
CB primary diameter during random filling	20	[nm]
Porosity of the catalyst layer	0.6093	[-]
Ionomers volume ratio	0.0695	[-]
I/C ratio	0.25	[-]
Catalyst layer overlap	0.20	[-]
Pt/C weight ratio	46.0	[wt %]
Standards platinum loading amount	0.2 /0.3 /0.5	[mg/cm^2]
CB density	1700	[kg/m^3]
Pt density	21450	[kg/m^3]
Pt particle diameter	5.0	[nm]

Table 2.5. Conditions of simulating CCL (macro-scale).

Property	Value	Units
Cell temperature	80	[°C]
Relative humidity	100	[%]
Ionomer distribution	Uniform	[-]
Supply oxygen percentage	0.21	[-]
PEM thickness	25.0	[μm]
GDL porosity	0.78	[-]
GDL curvature	4.00	[-]
GDL thickness	200.0	[μm]
Ionomer oxygen diffusion coefficient	8×10^{-12}	[m^2/s]
Ionomer oxygen dissolution constant	0.3125	[atm m^3/mol]
Cathode transfer factor	0.5	[-]
Water diffusion coefficient in PEM	5.5×10^{-11}	[m^2/s]
Density during film drying of membrane	1.1	[kg/m^3]
Molecular weight of the membrane	2000	[kg/mol]
Average pore diameter of catalyst layer	100	[μm]
Reference oxygen exchange current density	5.0×10^{-3}	[A/m^2]
Membrane resistance correction parameters	6.0	[-]
Pt oxidation adsorption energy parameters	3.0×10^{3}	[-]
Anode coefficient of Pt oxidation	0.25	[-]
Cathode coefficient of Pt oxidation	0.25	[-]
Oxidation potential of Pt	0.76	[V]
Diffusion coefficient correction factor	0.01	[-]

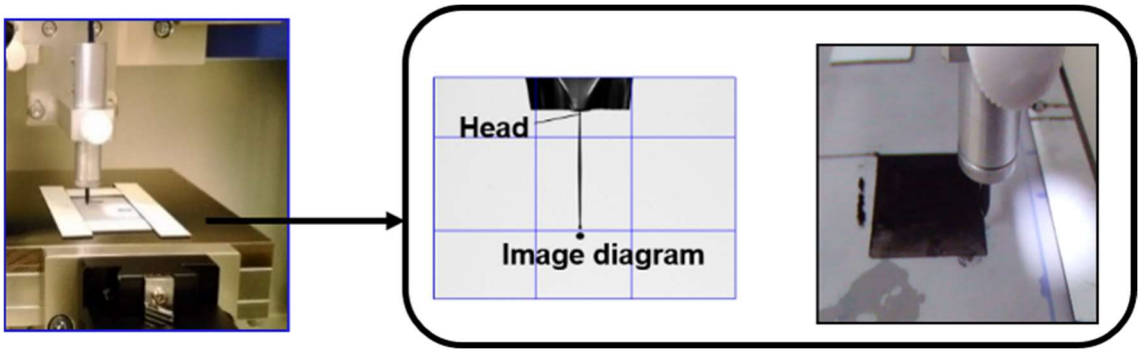

Fig. 2.1. Technology of inkjet.

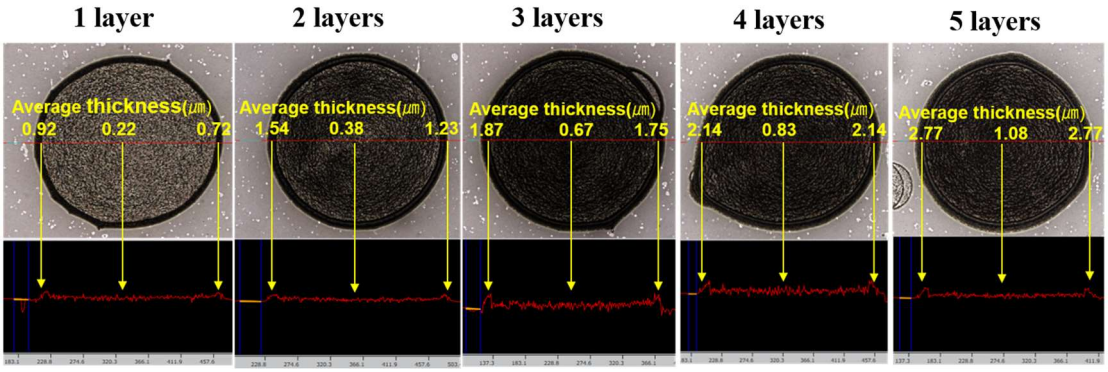

Fig. 2.2. Image of a drop ink per layer using laser microscope.

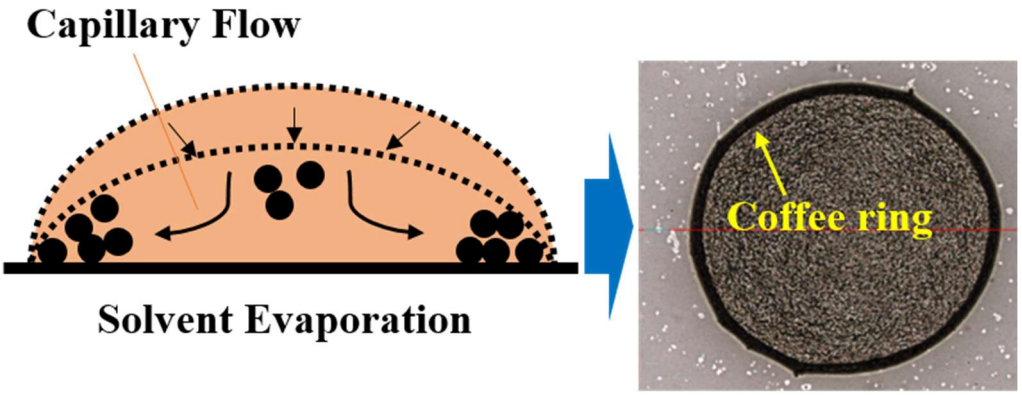

Fig. 2.3. Coffee ring effect.

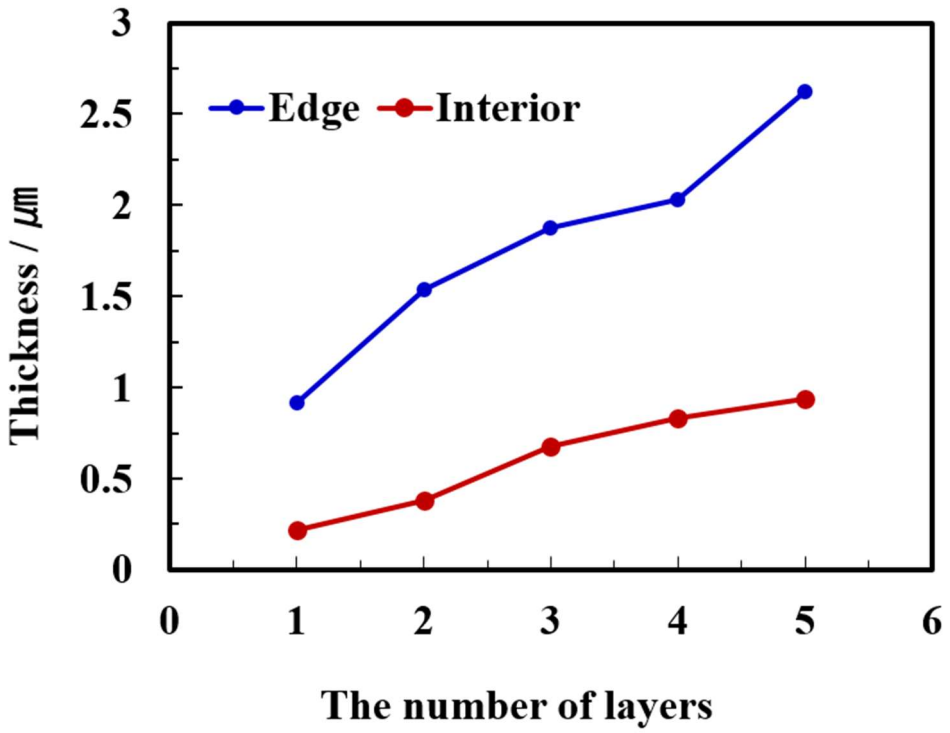

Fig. 2.4. Thickness of the interior and edge.

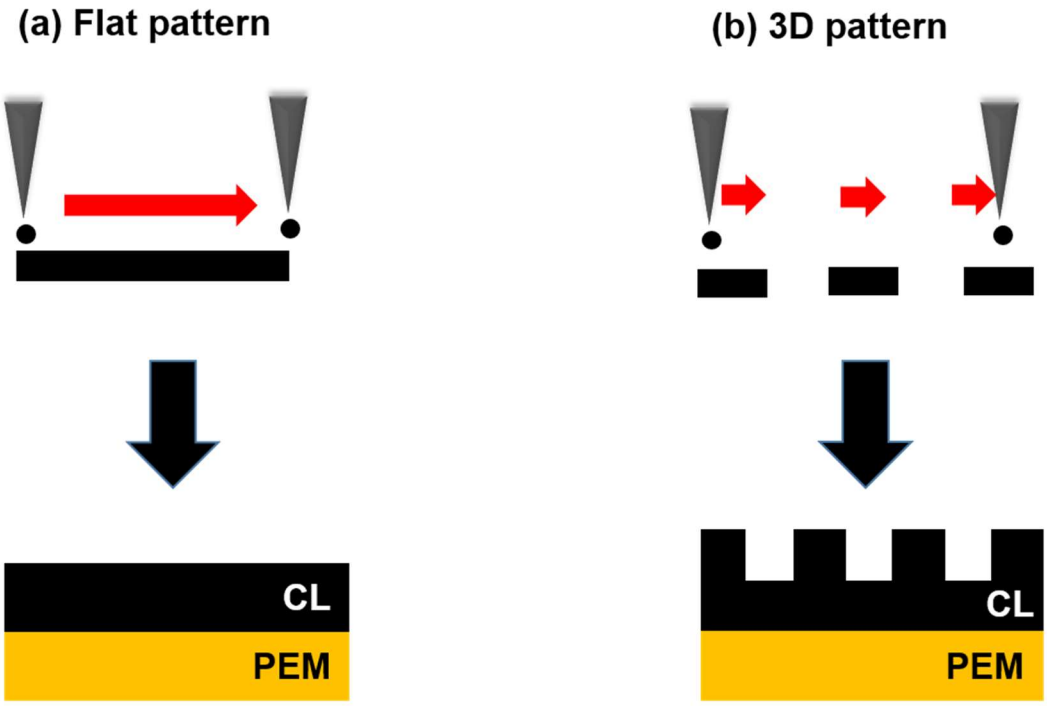

Fig. 2.5. The schematic of procedure of fabricated catalyst layer and cross section image (a) and ionomer layer and cross section image (b).

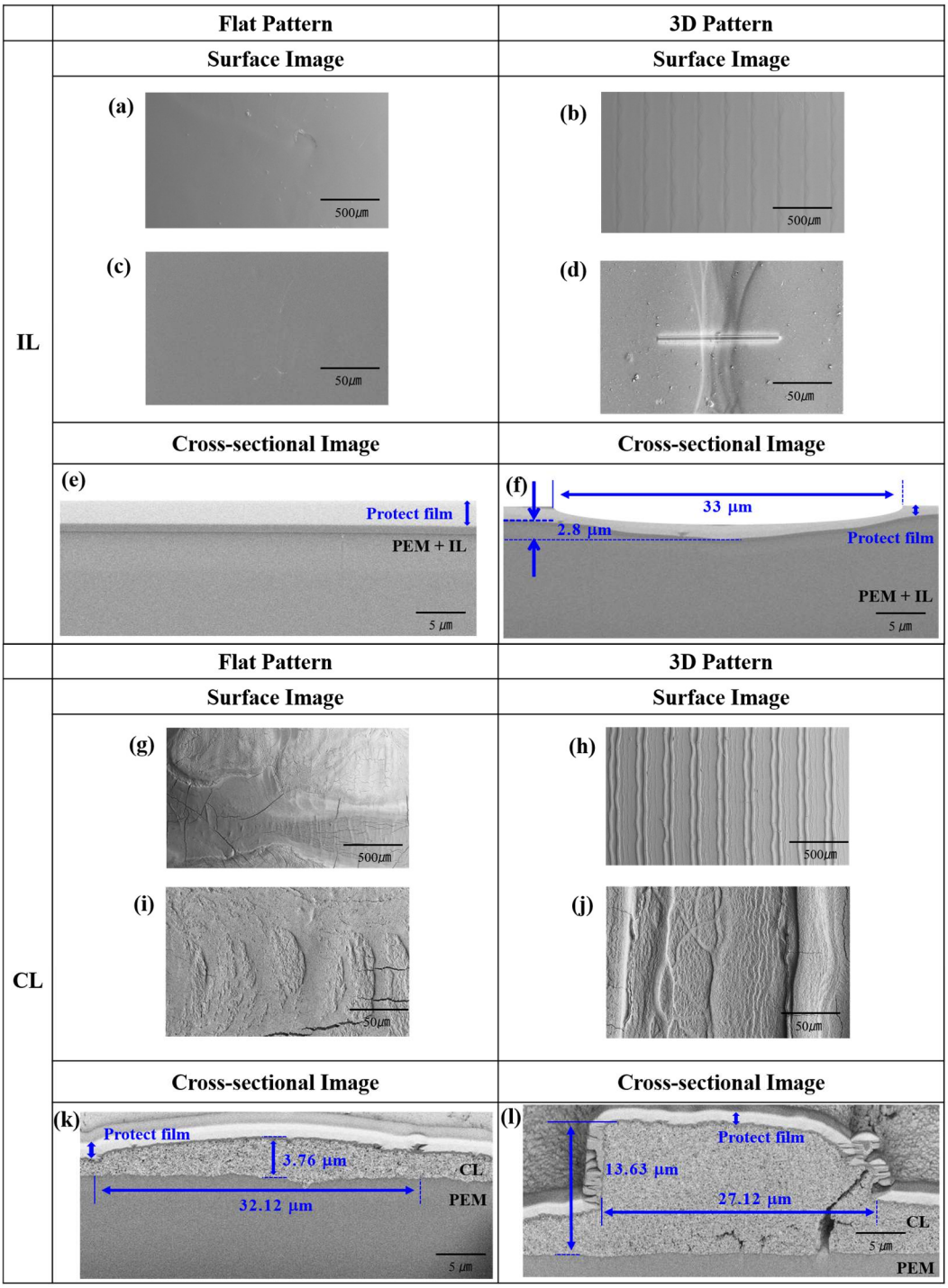

Fig. 2.6. Surface SEM images at 500 ㎛ (a, b, g, h) and 50 ㎛ (c, d, i, j) scales and cross-sectional (e, f, k, l) SEM images of flat- and 3D-patterned structure in each IL and CL.

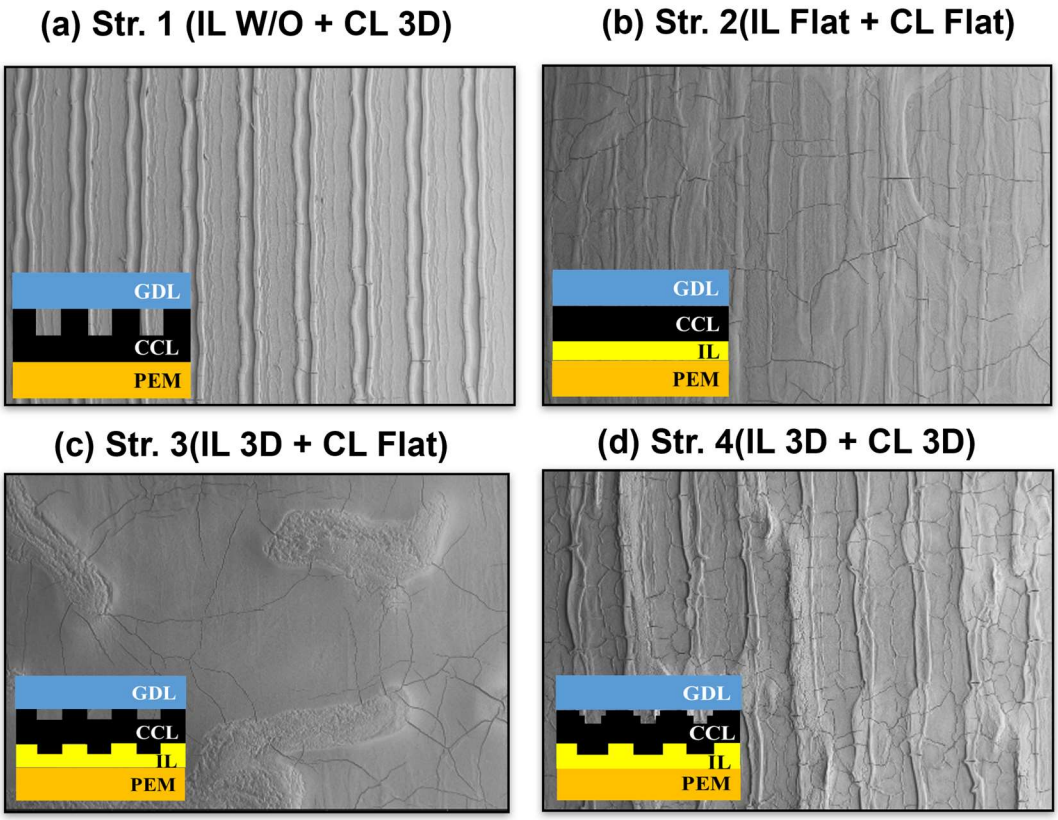

Fig. 2.7. Proposed structures and SEM images of the four types of 3D-patterned and flat-patterned structures fabricated using ionomer solution and catalyst ink that (a) Str.1 (ICL W/O+CL 3D), (b) Str.2 (ICL Flat+CL Flat), (c) Str.3 (ICL 3D+CL Flat) and (d) Str.4 (ICL 3D+CL 3D).

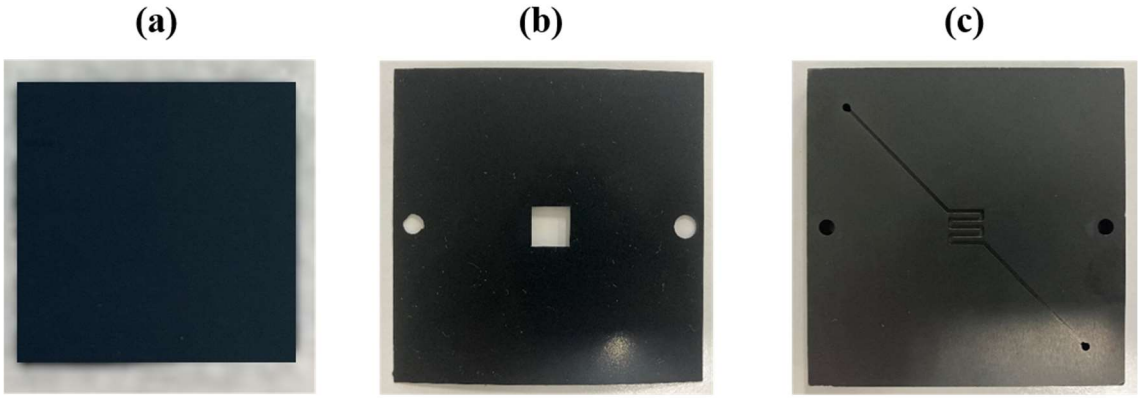

Fig. 2.8. Image of GDL (a), gasket (b) and serpentine (c) of single cell.

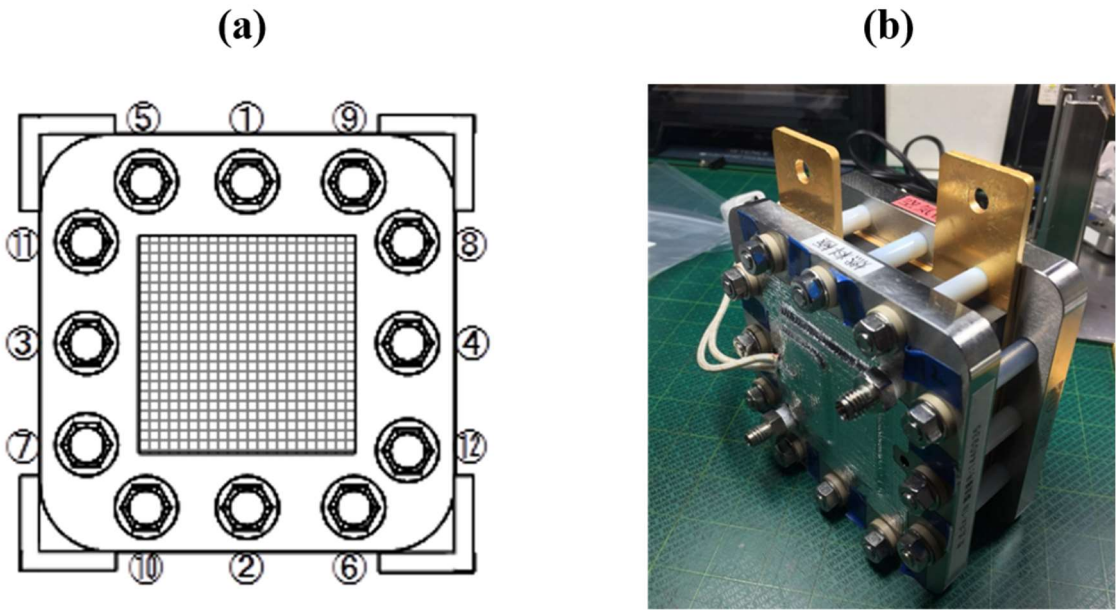

Fig. 2.9. Order of tightening cells (a), PEFC single cell (b).

Fig. 2.10. Fuel cell testing system.

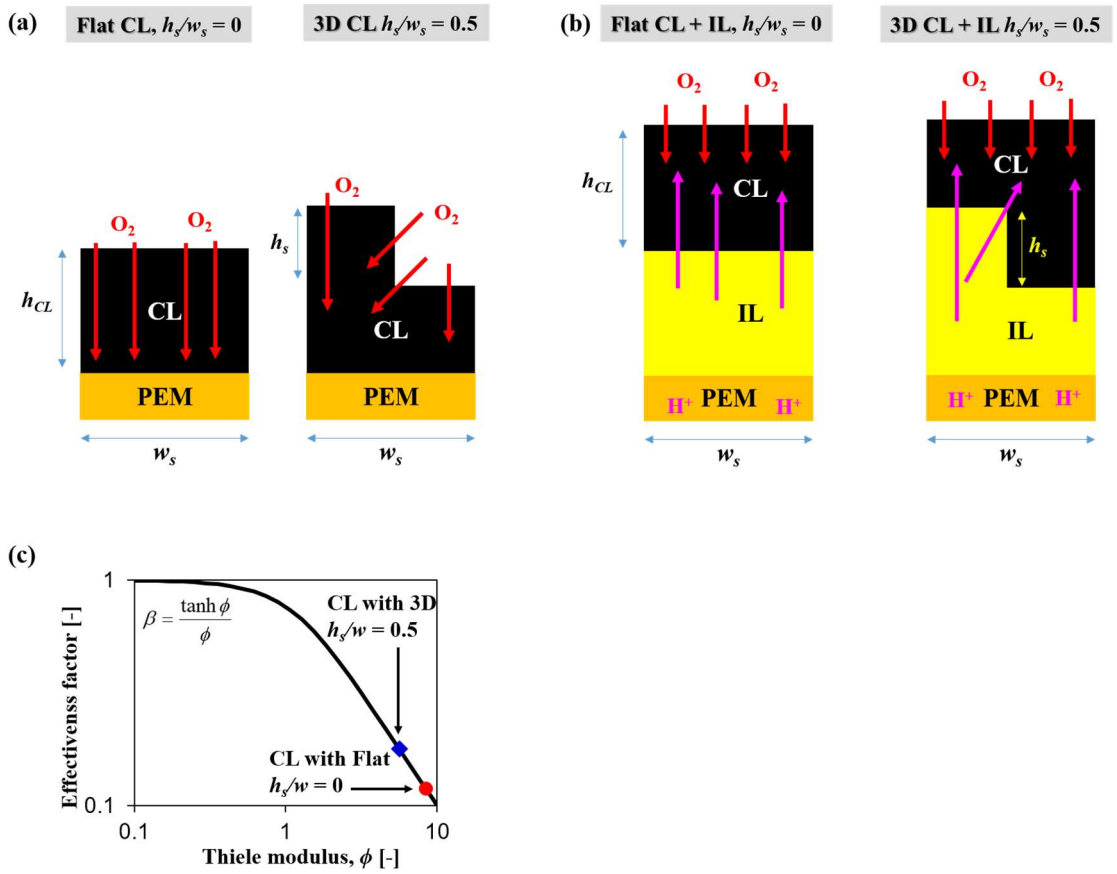

Fig. 2.11. Calculation of (a) the diffusion length of oxygen, (b) the diffusion length of proton and (c) the relationship between the effectiveness factor and the Thiele modulus of the CCLs with flat- and 3D-structures. Calculation of the conduction length of flat- or 3D-patterned IL structures.

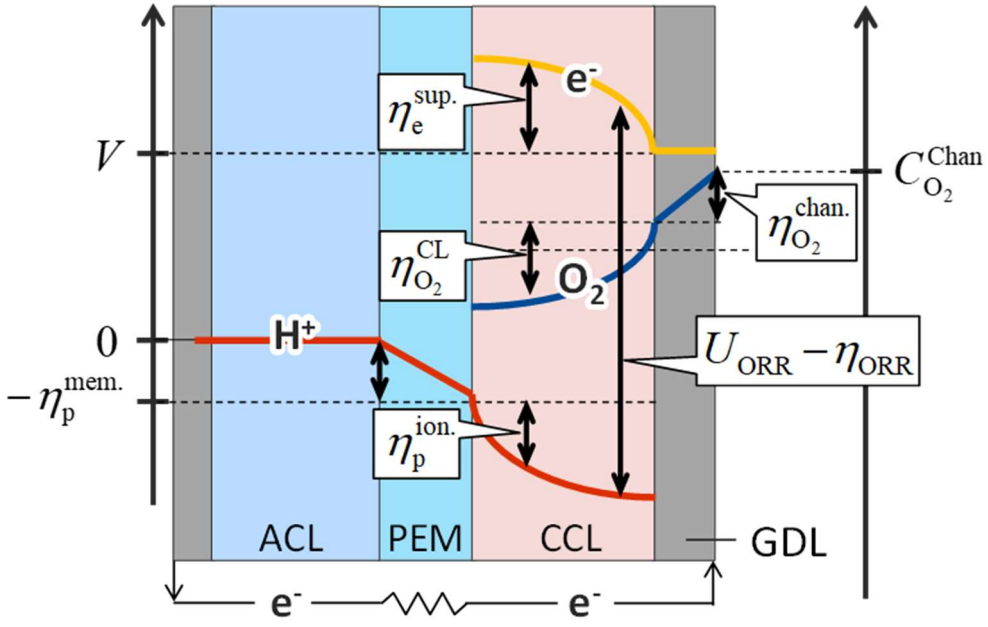

Fig. 2.12. Concept of overvoltage breakdown.

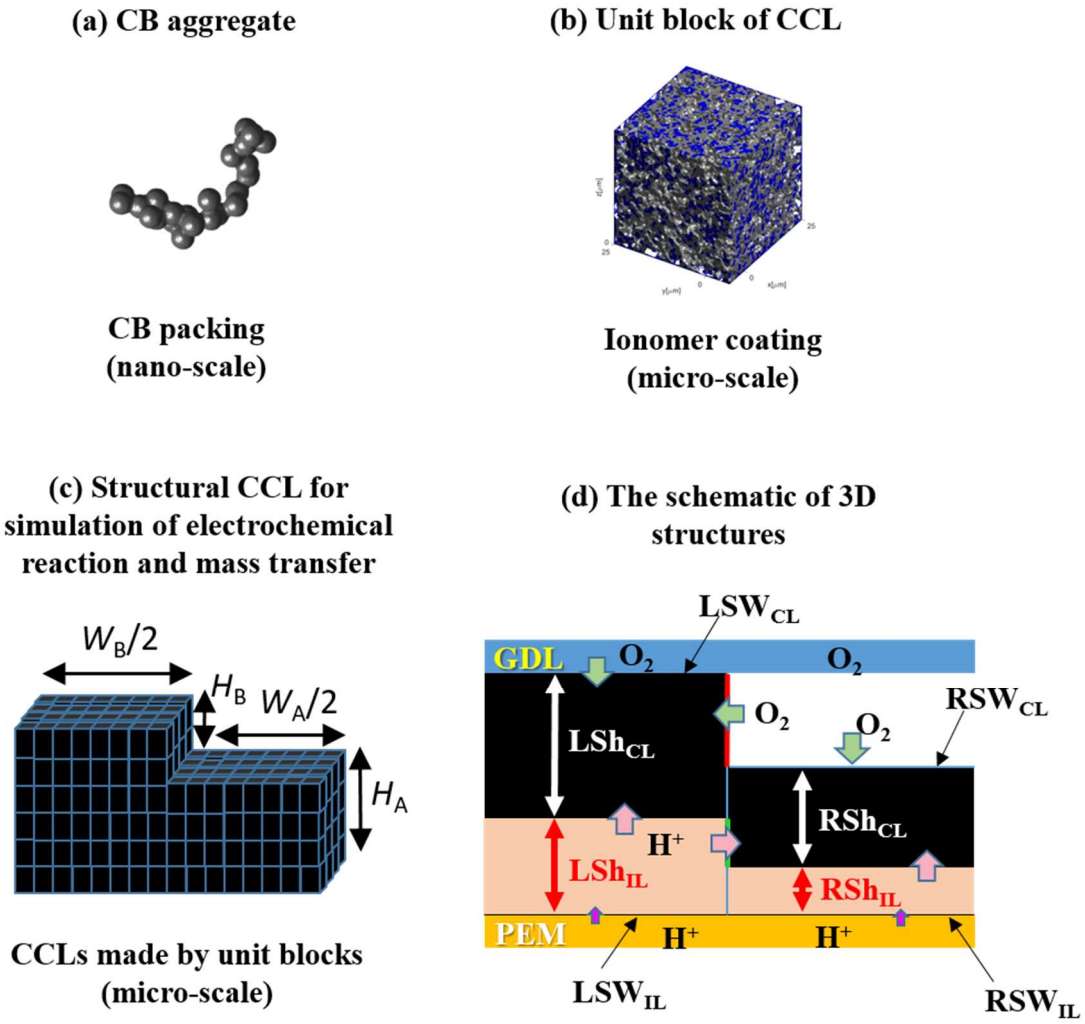

Fig. 2.13. Agglomeration of carbon (a), fabrication of unit catalyst layer (b), fabrication of structures, calculation of reactions (c) and schematic of 3D structures (d).

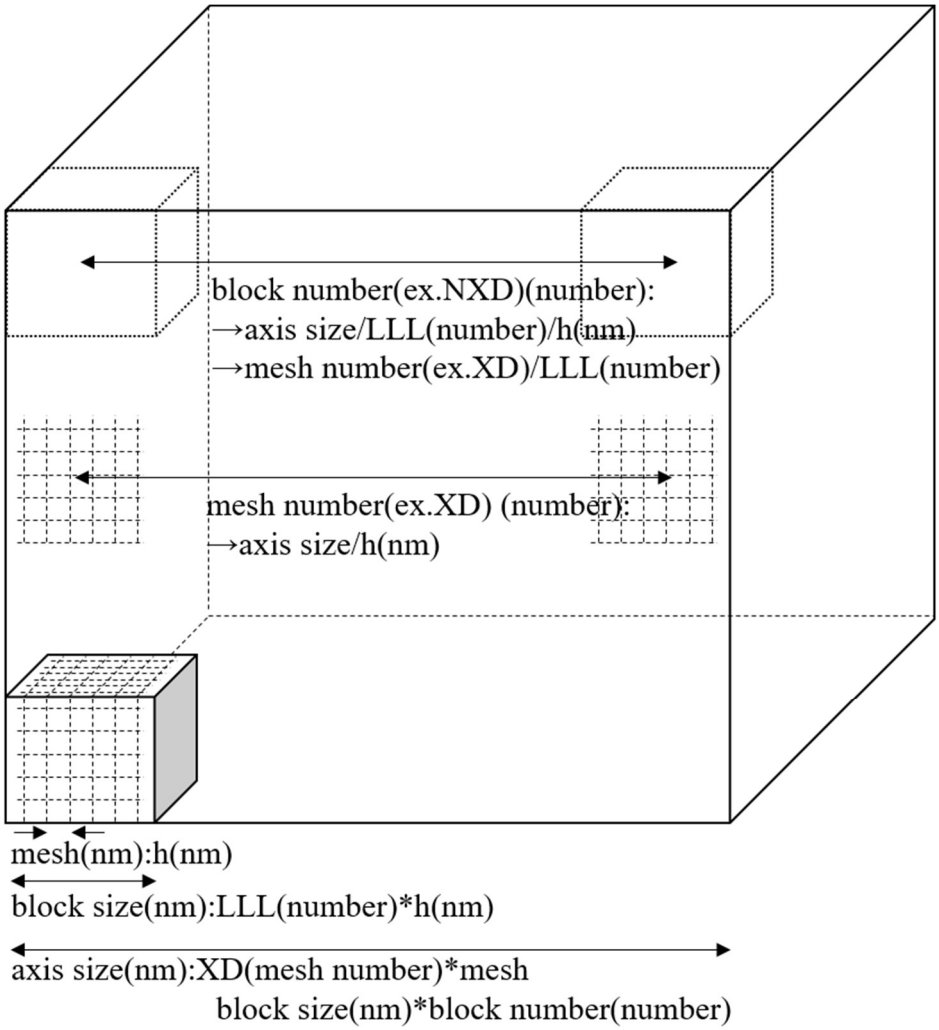

Fig. 2.14. Relationship between block number and thickness.

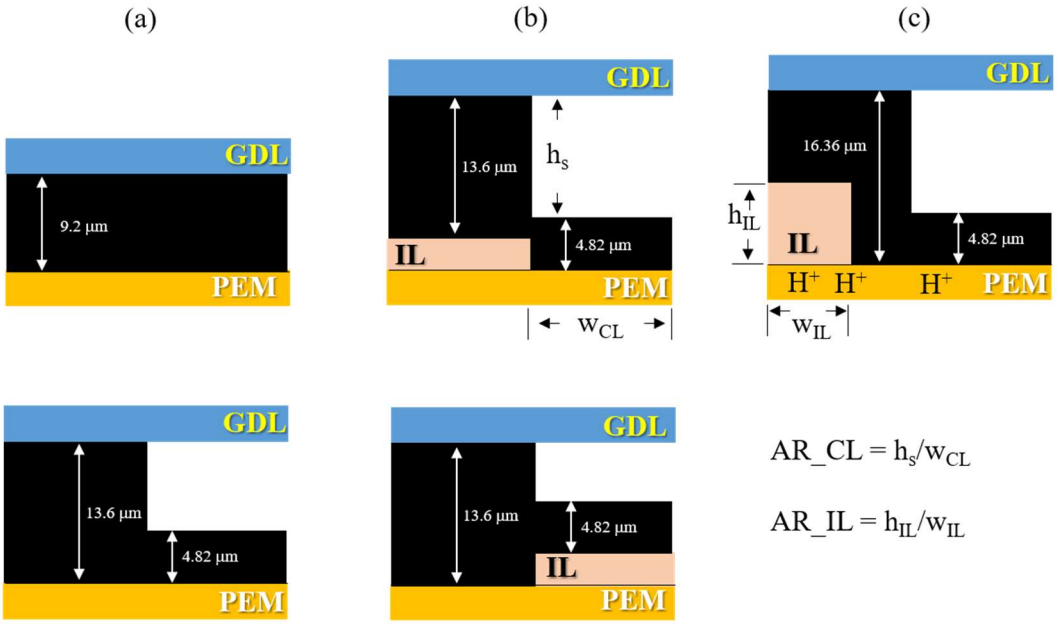

Fig. 2.15. The schematic of catalyst layer (a) flat and 3D structure without ionomer layer, (b) 3D structure with IL position of left and right side and (c) 3D structure various IL aspect ratio.

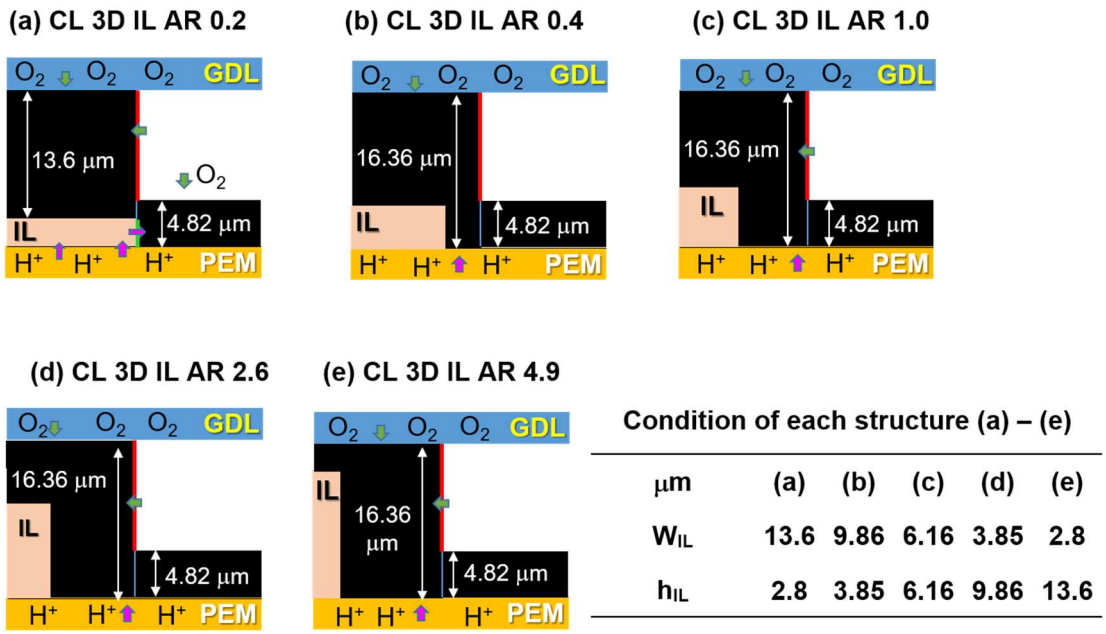

Condition of each structure (a) – (e)

μm	(a)	(b)	(c)	(d)	(e)
W_{IL}	13.6	9.86	6.16	3.85	2.8
h_{IL}	2.8	3.85	6.16	9.86	13.6

Fig. 2.16. The schematic of catalyst layer 3D pattern structure that different aspect ratio in ionomer layer CL 3D IL AR 0.2 (a), CL 3D IL AR 0.4 (b), CL 3D IL AR 1.0 (c), CL 3D IL AR 2.6 (d) and CL 3D IL AR 4.9 (e).

3. Result and Discussion

3.1 Experimental Results of Single and Double Side Catalyst Layer

The electrochemical characterization of the CCLs with four types of structures was performed at 80 ℃ and 100 % RH and 40 % RH. **Figure 3.1** shows the polarization curve and power densities of the CCLs at 100 % RH. Str. 1, Str. 2, and Str. 4 exhibited similar cell performance, while the performance of Str. 3 was lower than that of the other structures. This result indicates that the addition of the IL to the CCLs does not contribute to the improvement of cell performance at 100 % RH with sufficient proton conduction. In particular, the cell performance of Str. 3 was rather lower than that of Str. 1 after the addition of the 3D-patterned IL. This could be attributed to the amorphous agglomerates distributed on the flat surface of Str. 3 as shown in **Fig. 3.1**. Owing to the thick amorphous agglomerates, the mass transport resistance increases, resulting in a decrease in the cell performance. The power densities of the CCLs showed the same trend. The cell performance and maximum power density of the CCLs are summarized in **Fig. 3.2**. **Figure 3.2 (a)** shows a comparison of the cell performance of the CCLs at 0.6 V. The cell performance at 0.6 V, related to the ohmic resistance, increased in the order Str. 1 > Str. 2 > Str. 4 > Str. 3. On the other hand, the cell performance at 0.2 V, related to the mass transport such as oxygen transport, was almost same for Str. 1 and Str. 4 and decreased on moving from Str. 2 to Str. 3. In addition, the maximum power density showed the same trend as the cell performance at 0.2 V. **Figure 3.3** shows the polarization curve and power densities of the CCLs at 40 % RH. The cell performance and maximum power density of Str. 4 were considerably higher compared to those of the other CCLs at 40 % RH, at which proton conduction is usually poor. The cell performance at 0.6 V and 0.2 V and the maximum power density of the CCLs were compared in detail as shown in **Fig. 3.4**. The cell performance at 0.6 V improved two-folds after adding the 3D-patterned IL to Str. 1. Also, at 0.2 V, the cell performance of Str.4 improved by about 1.3 times compared to that of Str. 1. In addition, the maximum power density of Str. 4 also increased by at least 1.5 times compared to those of the other CCLs. These results suggest that the proton path in the CL of Str. 4 is shortened because the surface of the uneven IL and the surface of the CL are alternately curved.

However, the cell performance was not improved by increasing the proton conductivity for the other CCLs. Thus, even if the IL is added, the effect of the IL on the performance varies depending on the structural combination of the CL and IL in the CCLs.

To quantitatively analyze the relationship between the patterned structures and the resistance of the CCLs, EIS was performed. **Figure 3.5** shows the impedance spectra of the four CCLs. There are two semicircles in the Nyquist plots of the CCLs. The semicircle to the left is attributed to the resistance related to the electrolyte membrane. In general, the ohmic resistance is about 0.02 at 100 % RH but is higher at 40 % RH [1]. Thus, the ohmic resistance changes depending on the RH [2]. In particular, at low RH, the ohmic resistance becomes very high. Compared to other structures, Str. 4 exhibits a very small resistance related to the electrolyte membrane, which may indicate increased proton conduction in this structure. The semicircle to the right in the Nyquist plots of the CCLs represents the charge-transfer resistance at the cathode. Smaller the diameter of the semicircle, lower is the resistance of the CCL. The charge-transfer resistance at 0.6 V was the lowest for Str. 4 among all the CCLs. In particular, the charge-transfer resistance of Str. 4 is 0.6 times that of Str. 1 (without IL). This is consistent with the performance of the CCLs.

To confirm the effect of the patterned structures included in the CCLs on the mass transport of oxygen, the limiting current densities were measured at 80 ℃ and 95 % RH using 1 % oxygen gas. **Figure 3.6** shows the limiting current densities of the four CCLs. The oxygen-limiting current density was used to quantify the accessibility of oxygen to the catalyst. The limiting current densities of Str. 1 and Str. 4 were almost same and higher than those of the other CCLs. This suggested that the CLs with 3D-patterned structures included in these two CCLs affected the oxygen diffusivity. Based on the above results, it can be concluded that Str. 4 exhibited an excellent performance at a low humidity. Thus, an optimized structure with excellent proton conductivity and oxygen diffusivity, attributable to the curvature between the 3D surfaces of the IL and CL, was designed.

3.2 Simulation Results of Single and Double Side Catalyst Layer

3.2.1 Comparison between Simulation and Experimental Results

Before simulating all CCL structures proposed in this study, it is imperative to validate the numerical model using previous experimental data [3]. Specifically, the simulation model for the CL flat, CL 3D and CL 3D with IL was constructed to mirror the experimental setup. The platinum (Pt) loading was set at 0.3 mg/cm² and conducted at 80 °C [4-5]. A comparison of polarization curves between experimental and simulated results, shown in **Fig. 3.7**, revealed a remarkable quantitative and qualitative alignment with the experimental data. This compelling correspondence affirmed the capability of the simulation model to accurately predict cell performance within 3D structures with complex IL added. In the case of CL 3D, the improvement is due to the reduced mass transport resistance of oxygen which provides more surface area for oxygen entry compared to the single surface in the flat structure. With additional IL added to the CCL, cell performance further improves. This improvement may be related to the shortened conductive path of the protons from PEM to GDL side lead to the lower proton resistance induced by the additional IL. To achieve the optimal CCL design with IL that yields increased cell performance, we numerically analyzed the 3D-structured CCLs with IL in terms of position, aspect, and I/C ratio.

3.2.2. Evaluation of Configuration CCLs with IL

In the 3D configuration of the CCLs, the surface area accessible for oxygen varies with the aspect ratio of the 3D patterns. To explore this variability, we initially assessed different aspect ratios of the CL while keeping the aspect ratio of the ionomer layer constant. Additionally, the position of the IL was alternated from left to right, as depicted in **Fig. 3.8**. The performance of these configurations was evaluated under operational conditions of 100% relative humidity (RH) and 21% oxygen concentration (OC).

As illustrated in **Fig. 3.8**, configurations with the ionomer positioned on the left side of the catalyst layer (CL) consistently showed enhanced performance in terms of cell voltage and power density compared to those on the right side. This trend was observed across all three tested aspect ratios (AR)

of the CL. The presence of the ionomer layer on one side not only results in a thinner CL, which diminishes the resistance to oxygen diffusion but also provides a shortened proton pathway where IL is incorporated. Consequently, reactions occur at a higher rate on the side with IL, as demonstrated in **Fig. 3.8(b)**. In the cell performance evaluation conducted according to the three AR conditions of CL, the characteristics were not significantly different. Based on above results, the IL should be added to the thicker side of the CL to enhance the cell performance.

3.2.3 Optimization the Configurations of CCLs with IL

According to the above results, it is confirmed that the cell performance is improved when the IL is added to the 3D CCLs structured. As shortened conductive path of the protons from PEM to GDL side, proton resistance reduced. Therefore, it is necessary to optimize the IL to achieve the optimal cell performance by changing the aspect ratio (AR) of the IL. Additionally, since fuel cells are used in automobiles, they must demonstrate their dominant characteristics under varying environmental conditions. The 21 % and 10 % oxygen concentrations (OCs) were applied due to pressure changes at high and low altitudes, the cell performance comparison represented in **Fig. 3.9-11** at 100 % relative humidity (RH) condition. The cell performance with different ARs of IL were evaluated in terms of polarization curves, oxygen, proton, current density distribution and maximum power density. The AR of IL was defined as h_{IL}/w_{IL}, and ARs were set as 0.2, 0.4, 1.0, 2.6, and 4.9. The first evaluation was at 100 % RH and 21 % OC as shown in **Fig. 3.9**. In **Fig. 3.9 (a-b)**, the cell voltage improved as the AR of IL increased. As the proportion of AR of IL increased, the proton path decreased, and it can reach the surface of the long path of the CL resulting in uniform distribution of mass transport and improved the cell performance. As the path of proton decreased, the proton resistance in ionomer also decreased as shown in **Fig. 3.9 (c)**. In the current density distribution, as the AR of IL increased, the amount of current distributed to the CL surface gradually increased. It appears that the ion transport proceeds smoothly. There was no significance different in the oxygen concentration distribution based on the AR conditions of the IL. In the proton potential distribution, the structure with IL AR 4.9 showed the most uniform distribution, this means that protons move smoothly through the IL. All distributions

represented in **Fig. 3.10**. Second, the evaluation at 100 % RH and 10 % OC shown in **Fig. 3.11**. As the oxygen concentration decreases, the structure with IL AR 4.9 revealed the good cell performance. Third, in the **Fig. 3.12**, the evaluation at low RH condition (40 %). As the condition of RH is reduced, there is a limitation in the ion and mass transport, they cannot move freely within the CCLs. Accordingly, as the current increases, the resistance is excessively loaded on the catalyst layer and the voltage drops rapidly around the current density of 0.75 A/cm^2. In addition, as the RH decreases, the PEM resistance rapidly increases, however, even in this condition the structure with IL AR 4.9 still have dominant cell performance result than other conditions. From the above evaluation, it revealed that the optimum AR of IL in 3D CCLs structure is 4.9.

3.2.4 Evaluation of 3D Structure with IL According to Various I/C ratio

Furthermore, we investigated the effect of the optimized IL on the ionomer/carbon (I/C) ratio. The I/C ratio were set from 0.15 to 1.25, and the comparison of CL flat structure, CL 3D Structure and CL 3D IL AR 4.9 structure in the case of maximum power density, ionomer resistance in ionomer and polarization curve shown in **Fig. 3.13**. When the I/C ratio increased from 0.25 to 1.25, the maximum power density as shown in **Fig. 3.13 (a)**, the ionomer thickness in the CCLs tended to increase and the cell performance tended to decrease. As the aspect ratio of ionomer that CL 3D structure increased, maximum power density tended to have higher cell performance. This indicates that regardless of the I/C ratio, the 3D structure has higher performance than the flat structure and improves cell performance by optimizing the paths of mass transfer in CCLs with 3D structure. In **Fig. 3.13 (b)**, CL 3D IL AR 4.9 is better performance compare to CL flat and CL 3D structure. As the I/C ratio increased, the proton resistance in the ionomer of all structures decreased as expected, while oxygen transport resistance for the ionomer increased significantly. This indicates that as the amount of ionomer increases, the ionomer layer around the Pt particles thickens, resulting in inhibited diffusion transport of oxygen moving into the ionomer. As shown in **Fig. 3.13 (c)**, the CL 3D IL AR 4.9 enhance cell performance compare to CL flat and CL 3D structure. The improved performance may have been the result of the different mass transport states inside the CCLs because of add to IL in CCL.

Reference:

[1] Qayyum H, Tseng CJ, Huang TW, Chen SY. Pulsed laser deposition of platinum nanoparticles as a catalyst for high-performance PEM fuel cells. Catalysts 2016;6:1–13. https://doi.org/10.3390/catal6110180.

[2] Shukla, Shantanu, et al. "Effect of Ionomer Loading in Inket Printed Catalyst Coated Membranes on PEFC Performance." International Conference on Fuel Cell Science, Engineering and Technology. Vol. 44823. American Society of Mechanical Engineers, (2012).https://doi.org/10.1115/FuelCell2012-91152.

[3] Shukla S, Stanier D, Saha MS, Stumper J, Secanell M. Analysis of Inkjet Printed PEFC Electrodes with Varying Platinum Loading. J Electrochem Soc (2016);163:F677–87. https://doi.org/10.1149/2.1111607jes.

[4] Shukla S, Domican K, Secanell M. Analysis of Kinetic Parameters and Effect of Pt Loading on Cell Performance of PEFC Electrodes Prepared by Inkjet Printing. ECS Meet Abstr (2015);MA2015-02:1439–1439. https://doi.org/10.1149/ma.

[5] Fernández R, Ferreira-Aparicio P, Daza L. PEMFC electrode preparation: Influence of the solvent composition and evaporation rate on the catalytic layer microstructure. J Power Sources (2005);151:18–24. https://doi.org/10.1016/j.jpowsour.

[6] Noh T, Park K, Gao R, Kimura N, Inoue G, Tsuge Y. Effect of Double-Sided, 3D-Patterned Cathode Catalyst Layers on Polymer Electrolyte Fuel Cell Performance. Energies 2022;15. https://doi.org/10.3390/en15031179.

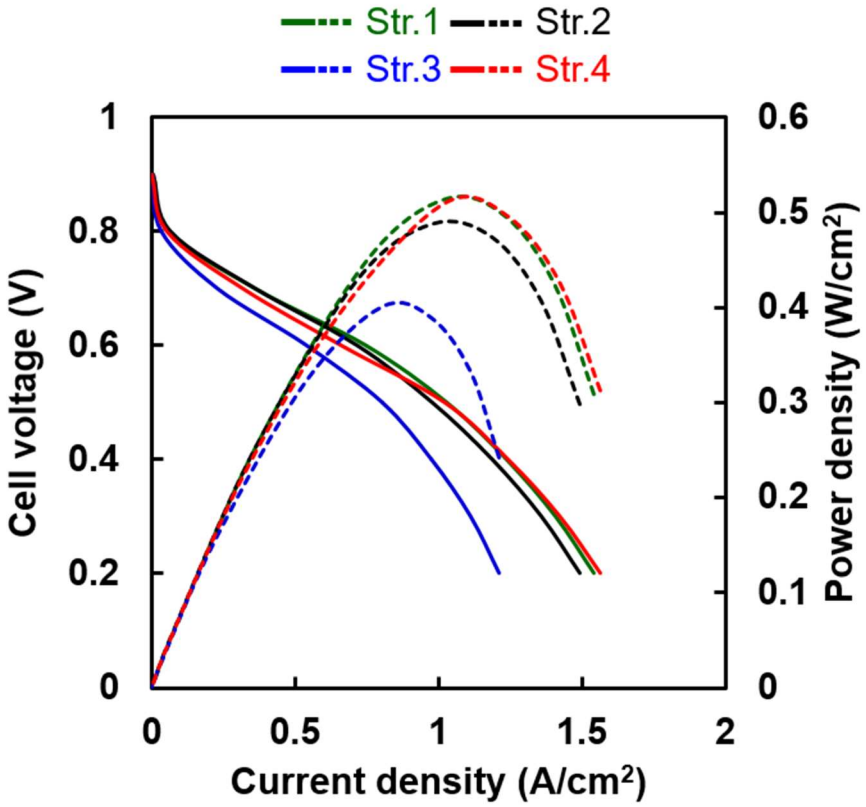

Fig. 3.1. Polarization curves and power densities of the four samples at 100 % RH and 21 % OC.

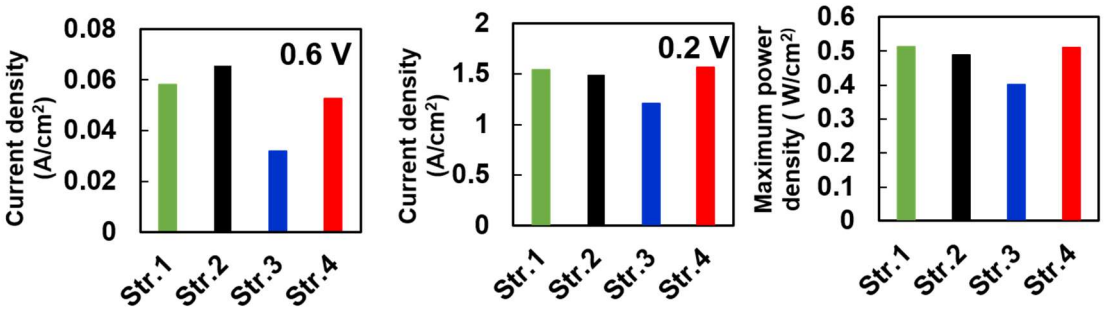

Fig. 3.2. Performance of the four CCLs at 0.6 V (a) and 0.2 V (b) and the maximum power density (c) at 100 % RH.

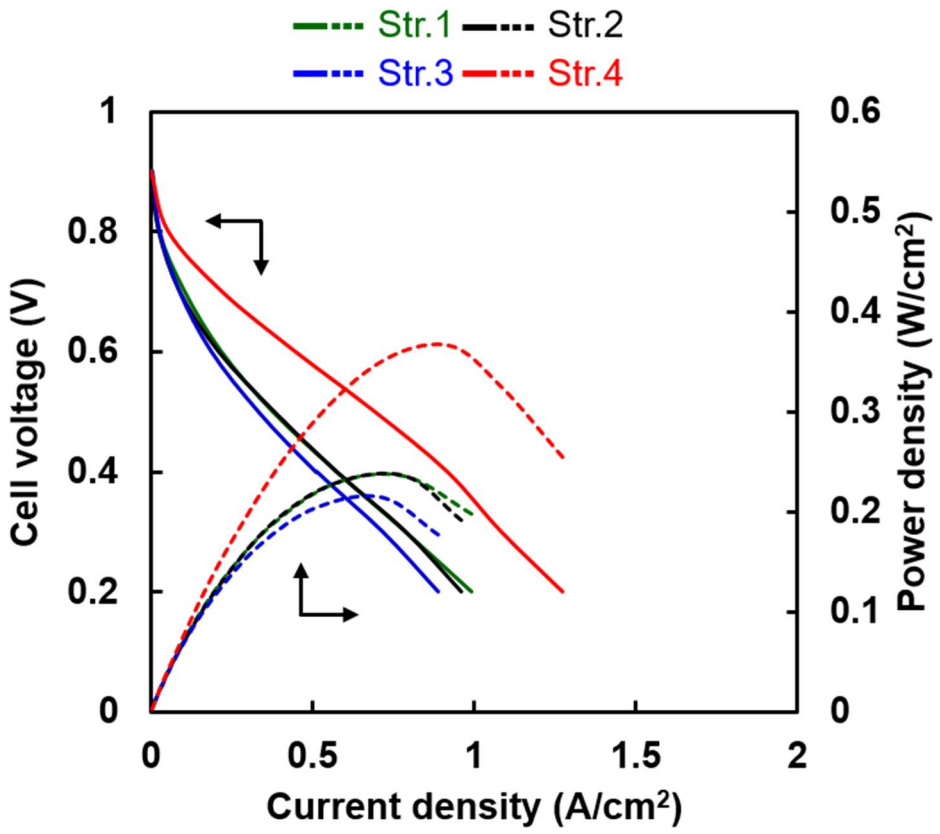

Fig. 3.3. (a) Polarization curves and (b) power densities of the four samples at 40 % RH.

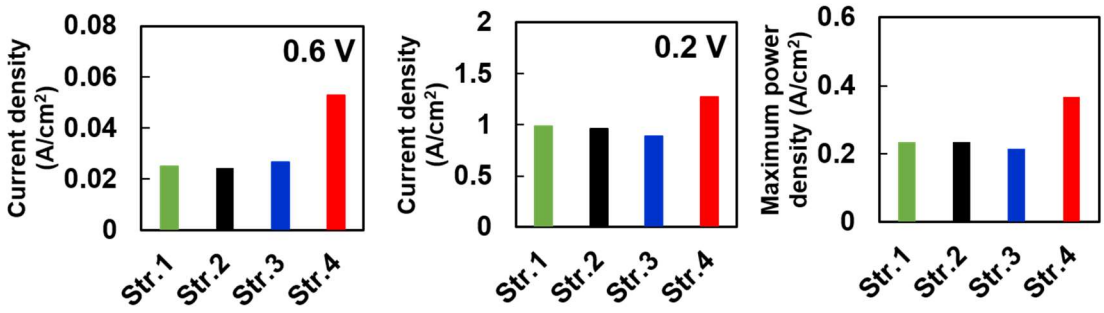

Fig. 3.4. Performance of the four CCLs at 0.6 V (a) and 0.2 V (b) and the maximum power density (c) at 40 % RH.

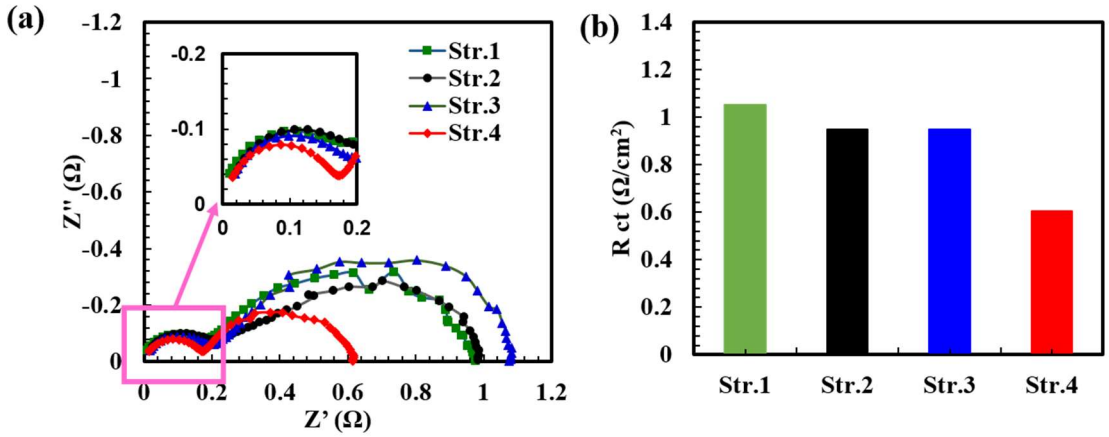

Fig. 3.5. Impedance spectra (a) and charge transfer resistances (b) of the four CCLs at 0.6 V, 80 ℃, and 40 % RH.

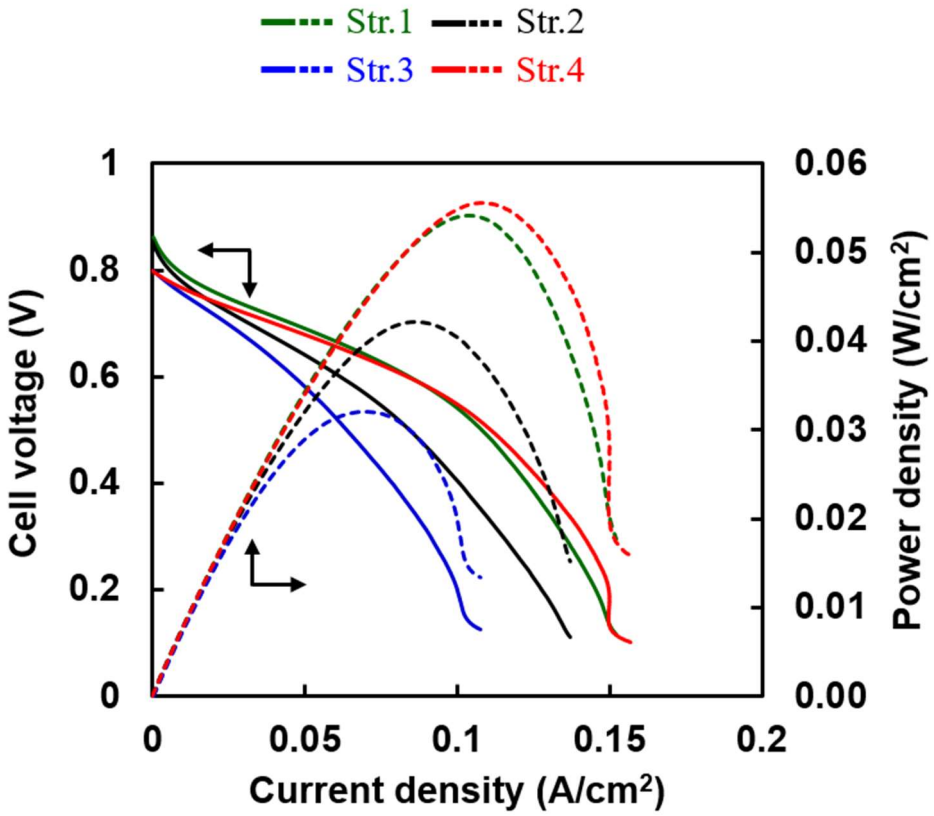

Fig. 3.6. Limiting current densities of the four CCLs using 1% oxygen gas at 80 ℃ and 95 % RH.

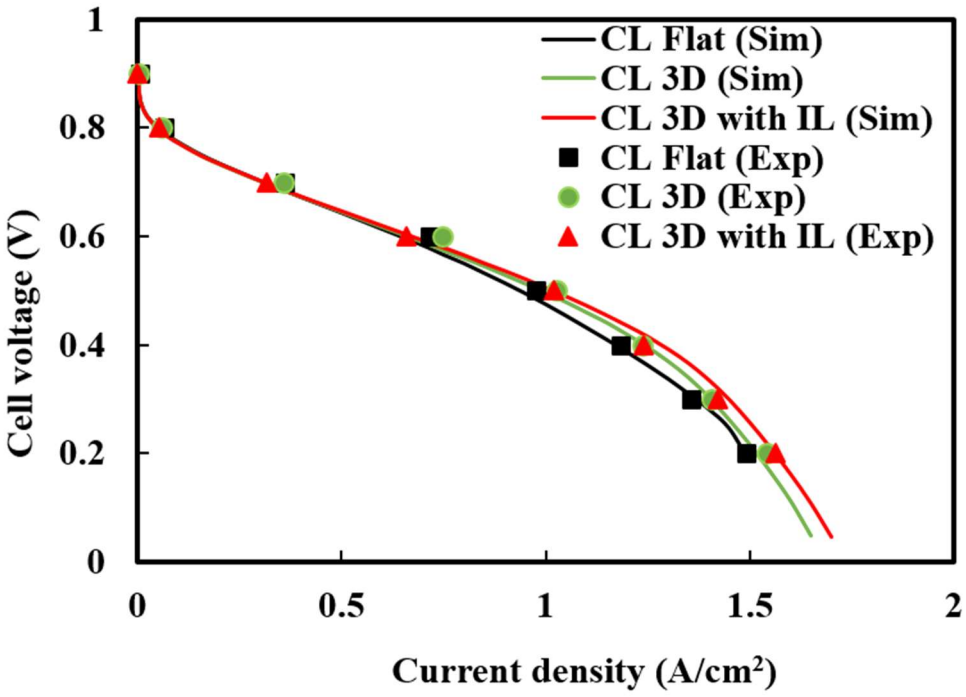

Fig. 3.7. Polarization curves from simulations and comparison with previous experimental results of Noh et al.[6] for 3D Flat, CL 3D and CL 3D with IL at platinum (Pt) loadings of 0.3 mg/cm^2.

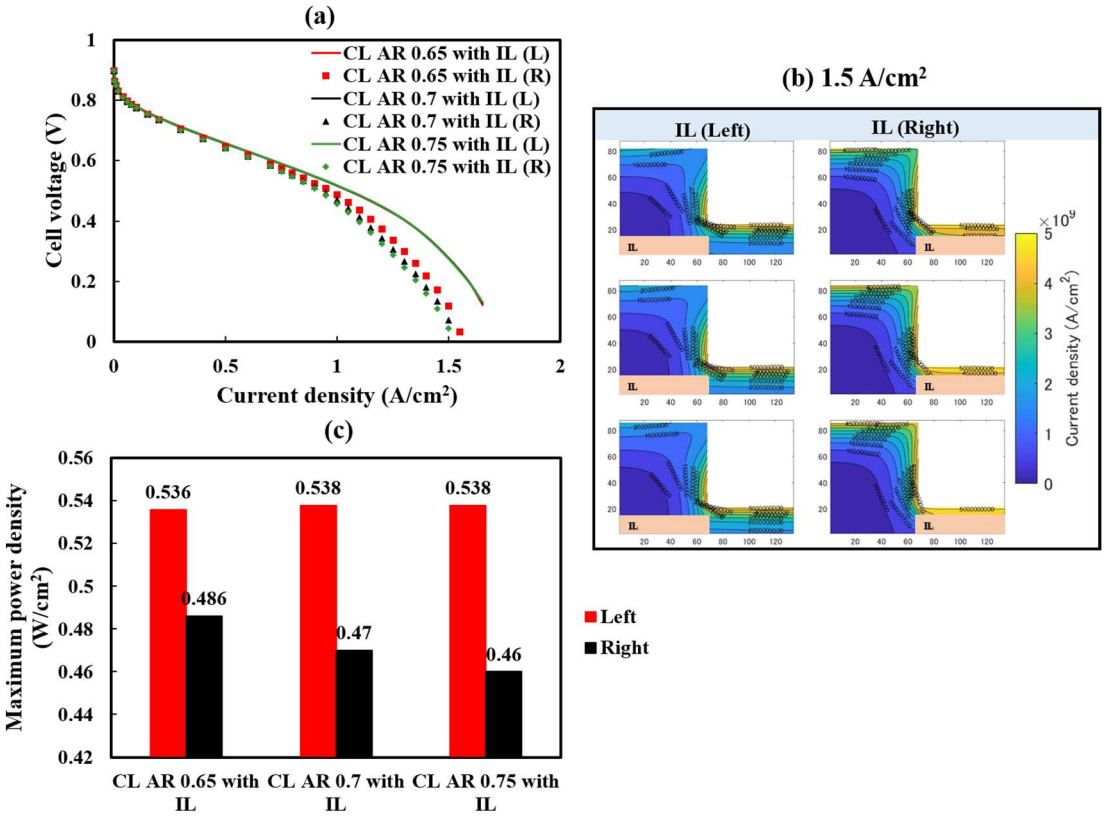

Fig. 3.8. Evaluation of CL 3D with IL structural CCLs with various CL aspect ratio at 100 % RH and 21 % OC: (a) Polarization curves, (b) current density distribution and (c) maximum power density of overvoltage at 1.5 A/cm^2.

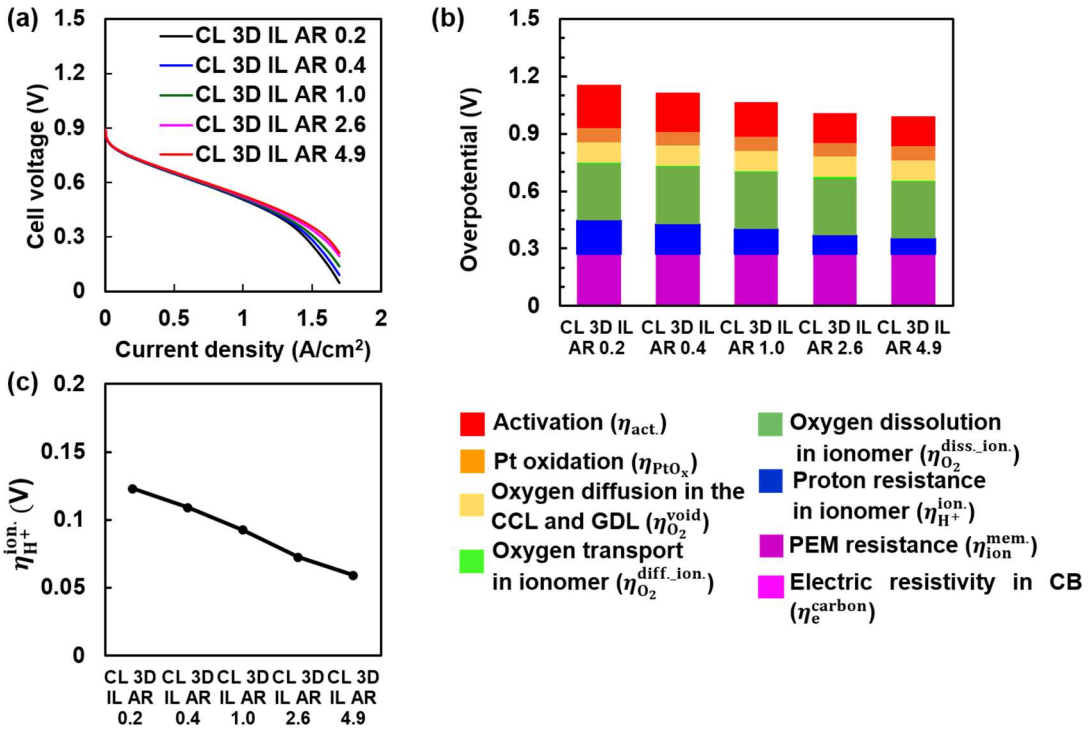

Fig. 3.9. Evaluation of CL 3D with IL structural CCLs with various aspect ratio at 100 % RH and 21 % OC: Polarization curves (a), bar diagrams of overvoltage at 1.7 A/cm^2 (b) and proton resistance in ionomer (c).

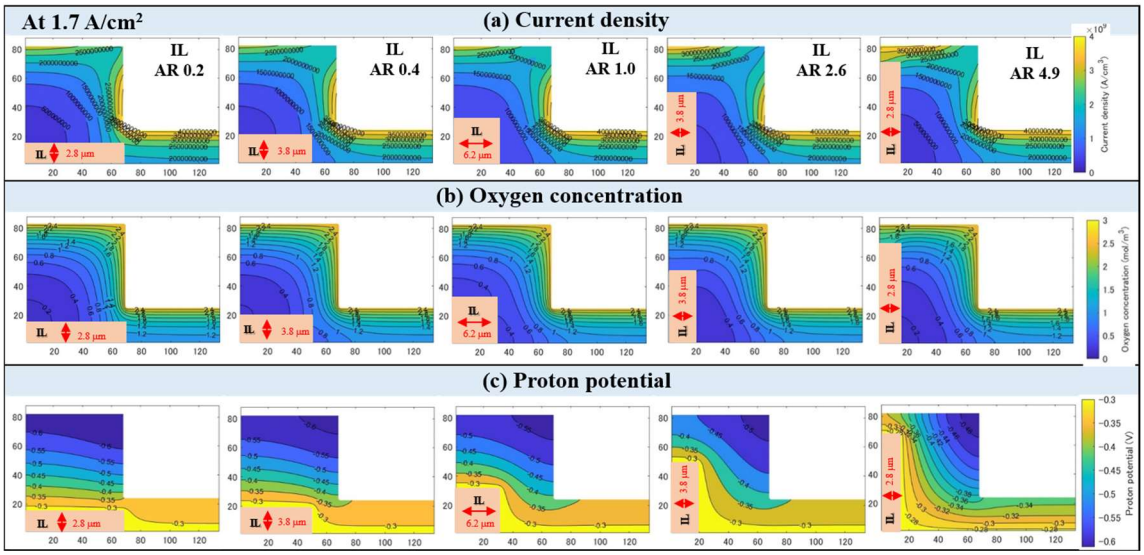

Fig. 3.10. Distribution of current density (a), oxygen concentration (b) and proton potential (c) CL 3D with IL structural CCLs with various aspect ratio at 100 % RH and 21 % OC of overvoltage at 1.7 A/cm^2.

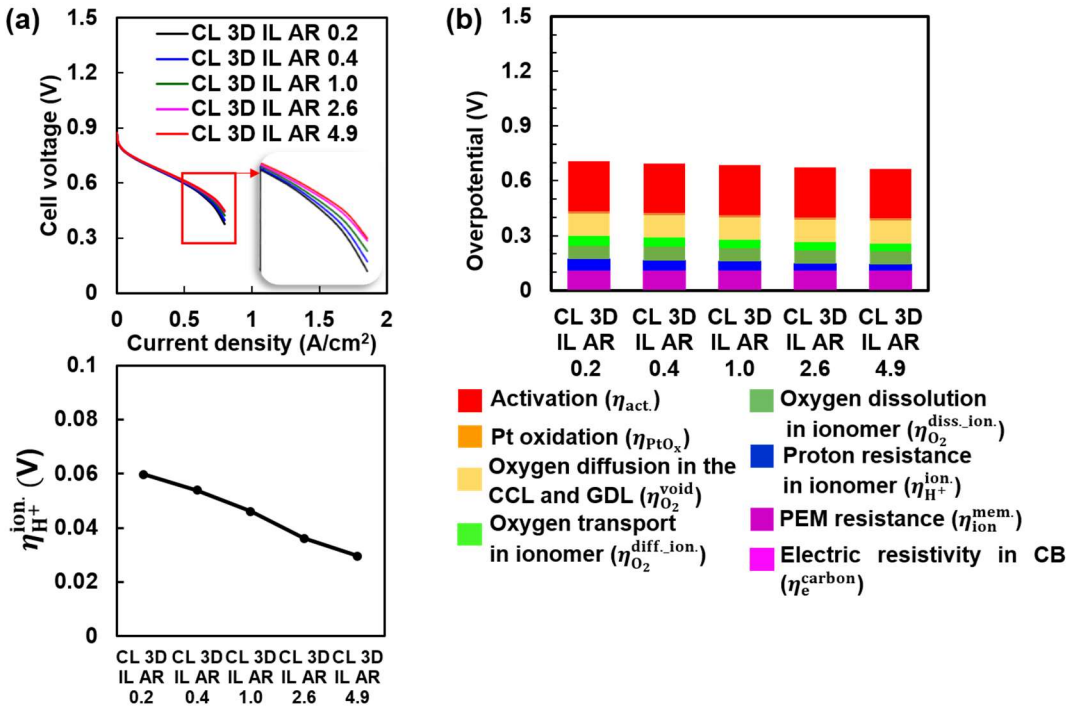

Fig. 3.11. Evaluation of CL 3D with IL structural CCLs with various aspect ratio at 100 % RH and 10 % OC: Polarization curves (a), bar diagrams of overvoltage at 0.8 A/cm^2 (b) and proton resistance in ionomer (c).

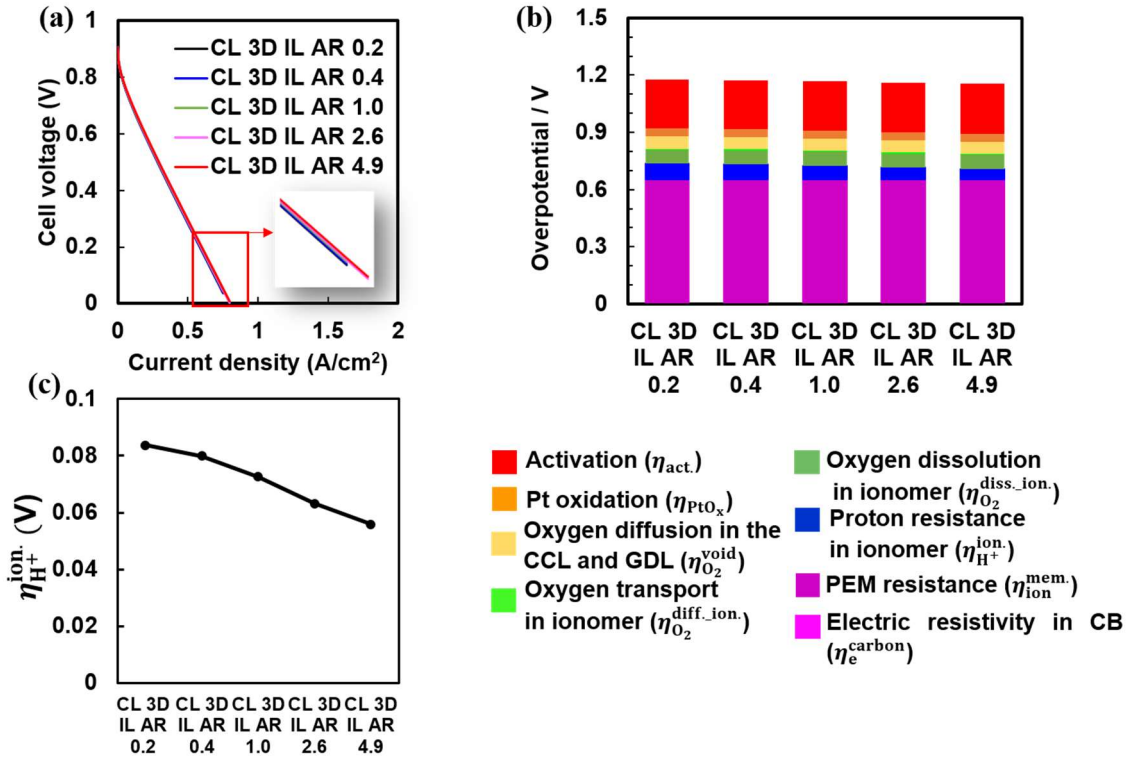

Fig. 3.12. Evaluation of CL 3D with IL structural CCLs with various aspect ratio at 40 % RH and 21 % OC: Polarization curves (a), bar diagrams of overvoltage at 0.75 A/cm^2 (b) and proton resistance in ionomer (c).

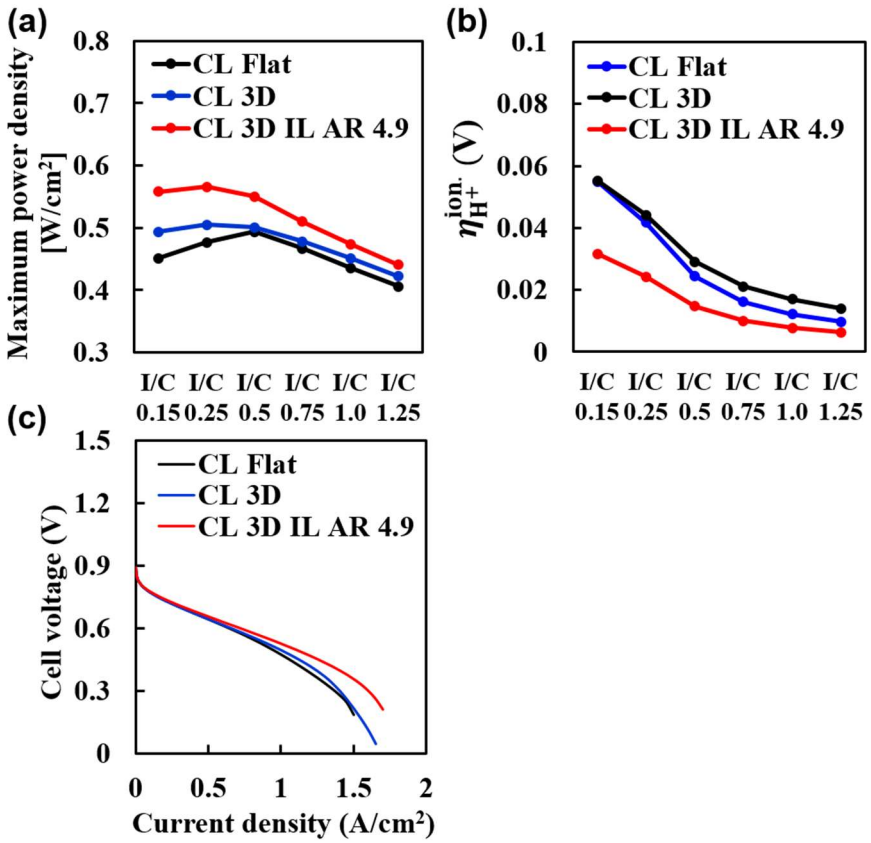

Fig. 3.13. Evaluation of CL flat, CL 3D and CL 3D with IL AR 4.9 structure with various I/C ratio at 100 % RH and 21 % OC: maximum power density (a), proton resistance in ionomer (b) and polarization curve (c).

4. Conclusion and Future study

4.1 Summary and Conclusion

Polymer electrolyte fuel cells (PEFCs) are gaining significant attention due to their high output density, fast start-up time, and ability to operate efficiently at both cold and room temperatures. However, PEFCs face significant challenges, primarily due to the high costs associated with using platinum (Pt) as a catalyst. The oxygen reduction reaction (ORR) proceeds more slowly at the cathode, necessitating a large amount of platinum. To improve ORR performance, rather than increasing the amount of Pt used, the supply of oxygen, protons, and electrons should be smooth, quick, and uniform. Previous researchers have explored various methods to increase ORR by developing new materials and enhancing oxygen diffusion to the catalyst layer (CL) by modifying its structure. However, methods to simultaneously improve oxygen diffusion and proton conductivity have not yet been explored.

This dissertation aims to enhance the performance of PEFCs by improving oxygen diffusion and ion conduction paths through experiments and simulations. Experimentally, inkjet technology, specifically the coffee ring technique, was employed to fabricate 3D cathode catalyst layers (CCLs), with and without an additional ionomer layer (IL). To optimize these structures, numerical simulations were performed to predict the characteristics of electrochemical reactions and mass transport, providing insights into the optimal design of the CCLs. The main conclusions are as follows:

Chapter 1 introduces the characteristics and applications of PEFCs and explores the importance of oxygen diffusion and proton conduction in enhancing ORR. The objective of this dissertation is also stated.

Chapter 2 details the fabrication process of the catalyst layer with flat and 3D patterns using the inkjet printing technique. Four types of structures with different configurations were fabricated to evaluate cell performance. The chapter also describes the numerical approach used to optimize the CCL structure, involving theoretical and reaction equations as the foundational basis for the simulation study. Five different types of CCL structures with varying aspect ratios of IL are proposed and

simulated to find the optimized 3D double-sided structure.

Chapter 3 presents and discusses the results of experiments and simulations. In the experimental part, theoretical equations were used to confirm that the shorter path of proton conduction in an IL with a 3D-patterned structure could improve cell performance, surpassing that obtained with a flat-patterned IL. The experimental investigation focused on the effect of the 3D-patterned IL included in the CCLs on cell performance. Str. 4 (IL 3D + CL 3D) showed excellent properties under 100 % relative humidity (RH) conditions. It was confirmed that the addition of IL to the CCLs did not contribute to cell performance improvement under 100 % RH conditions, where sufficient proton conduction was possible. The cell performance of Str. 4 was also higher than the others at 40 % RH. The results indicated that Str. 4 enhanced proton conductivity at low humidity, where proton conduction was poor, thereby improving cell performance. The electrolyte membrane-related resistance of Str. 4 was considerably lower than that of the other structures, which could be correlated to increased proton conduction.

In the simulation part, the validation of the simulation model against experimental results showed good agreement. After validation, the simulation model was employed to identify the best configuration. In particular, when the ionomer was added to the left of the CCL, cell performance was higher than when added to the right. As the aspect ratio of the ionomer increased, performance improved because the protons from the PEM to the ionomer were conducted closest to the surface of the CL, and protons were evenly distributed from the IL to the CL. Thus, the IL aspect ratio of 4.9 showed superior characteristics under different relative humidity and oxygen concentration conditions. The influence of the ionomer/carbon (I/C) ratio in double-sided 3D CCLs was also investigated, revealing that an I/C ratio of 0.25 showed the best performance.

Chapter 4 presents a concise conclusion and outlines future research directions. In conclusion, this study offers a method to enhance cell performance while reducing Pt usage through inkjet printing. It also provides valuable insights into optimizing performance through a simulation approach.

4.2 Future Study

In this study, 3D patterns were applied to the catalyst layer to reduce Pt loading, and an ionomer layer (IL) was positioned between the proton exchange membrane (PEM) and the gas diffusion layer (GDL) to improve oxygen diffusion and proton conduction. To further increase cell performance, additional methods were explored to optimize the structural design. These included using various carbon materials to fabricate the membrane electrode assembly (MEA), employing different fabrication techniques such as spray coating and brush painting for the cathode catalyst layer, and incorporating novel materials to enhance platinum utilization and the supply of protons, electrons, and oxygen to the Pt surface.

Acknowledgments

As I write this, my heart is filled with mixed emotions. I would like to thank the people who have encouraged and supported me during my Ph.D program at Kyushu University.

First, I would like to express my sincere gratitude to Dr. Gen Inoue, Professor of Chemical Engineering at Kyushu University. He guided me in all aspects of my research life, including my research student activities during the COVID-19 period. He taught me how to look at things from different perspectives and the scientific and logical aspects of research. He also sincerely guided me when I had difficulties.

I am very grateful to Dr. Takeru Yano, an assistant professor in the Department of Chemical Engineering at Kyushu University, for his support.

I would also like to thank the members of my lab, Dr. Magnus So, Dr. Nguyen Van Lap, and Dr. Agnesia Permatasari. I would also like to thank my former lab mates, Dr. Ka Young Park, Dr. Pham Thi Dung, Ms. Wei Yuting and Ms. Gao Ruijing. With their help, I was able to complete the experimental part and the overall research on simulation.

I sincerely thank all the staff and members of Lab 7 for their cooperation and help. They have helped me a lot in both research and daily life.

Finally, I would like to express my sincere gratitude to my family and all the members of Fukuoka Vision Church, including Pastor Ju Young Kim and Jesus, for their love and support.

2024.07.16

TAE HYOUNG NOH